ARTICLE IN PRESS
ATMOS-03032; No of Pages 20
Atmospheric Research 140 (2014) xxx–xxx

Contents lists available at ScienceDirect

Atmospheric Research

journal homepage: www.elsevier.com/locate/atmos

The horizontal space–time scaling and cascade structure of the atmosphere and satellite radiances

J. Pinel [a], S. Lovejoy [a,*], D. Schertzer [b]

[a] Physics, McGill University, Montreal, Quebec, Canada
[b] LEESU, Ecole des Ponts ParisTech, Université Paris-Est, Marne-la-Vallée, France

ARTICLE INFO

Article history:
Received 1 April 2013
Received in revised form 5 November 2013
Accepted 23 November 2013
Available online 4 December 2013

Keywords:
Turbulence
Scaling
Multifractals

ABSTRACT

Classically, turbulence has been modeled by a hierarchy of different isotropic scaling regimes. However, gravity acts at all scales and theory and modern observations point towards an atmosphere described by a single anisotropic scaling regime with different scaling laws in the horizontal and vertical directions: the 23/9D model. However, the implications of this anisotropic spatial scaling for the temporal statistics (i.e. the full space–time scaling) have not been worked out and are the subject of this paper. Small structures are advected by larger turbulent structures, by considering averages over the latter we obtain estimates for the structure functions and spectra.

To test these predictions, we analyze geostationary satellite MTSAT Infra red radiances over wide scale ranges in both horizontal space and in time (5 km to ~10000 km, 1 h to 2 months). We find that our model accurately reproduces the full 3D (k_x, k_y, ω) spectral density ~~over the range studied 60–~~5000 km in space and ~~2–~~100 h. For example, to within constant factors, the 1D spectral exponents were the same in both horizontal directions and in time with spectral exponent $\beta \sim 1.55 \pm 0.01$. We also considered the various 2-D subspaces ((k_x, k_y), (k_x, ω), (k_y, ω)) and showed how these could be used to determine both mean advection vectors (useful for atmospheric motion vectors) but also the turbulent winds.

Going beyond these second order statistics we tested the predictions of multiplicative cascade models by estimating turbulent fluxes from both MTSAT but also the polar orbiting TRMM satellite at infrared and passive microwave bands over scale ranges 100 km to 20000 km, 1 day to 1 year. These accurately obeyed the predictions of multiplicative cascade models over large ranges of spatial scales with typically slight deviations at smallest and largest scales. Analogous temporal analyses showed similar agreement at small scales, but with significant deviations at scales larger than a few days, marking two regimes, associated with weather and macroweather. This allows us to determine Eulerian frame space–time diagrams relating the sizes and lifetimes of structures.

1. Introduction

Turbulent flows have long been recognized for their complexity, randomness and myriad of structures of different sizes and lifetimes. Typically, one describes the statistics of the corresponding fluctuations with the help of scaling laws. For instance, the celebrated Kolmogorov law (Kolmogorov, 1941) describes how turbulent wind fluctuations change with scale. In real space, this law has the form: $\Delta v = \varepsilon^{1/3} \Delta x^{H}$ where Δv is a fluctuation in the turbulent wind field v, Δx is the spatial separation over which Δv is calculated, H is the mean fluctuation scaling exponent and ε is the flux of energy from large to small scales. The Kolmogorov law applies to statistically isotropic turbulence in three spatial dimensions and the dimensional arguments based on a homogeneous energy flux from large to small scales yield $H = 1/3$. We can also express these laws in Fourier space where they follow $E(k) = \varepsilon^{2/3} k^{-\beta}$ where $E(k)$ is

---

[*] Corresponding author.
E-mail address: lovejoy@physics.mcgill.ca (S. Lovejoy).

0169-8095/$ – see front matter © 2013 Elsevier B.V. All rights reserved.
http://dx.doi.org/10.1016/j.atmosres.2013.11.022

Please cite this article as: Pinel, J., et al., The horizontal space–time scaling and cascade structure of the atmosphere and satellite radiances, Atmos. Res. (2014), http://dx.doi.org/10.1016/j.atmosres.2013.11.022

the power spectrum of the turbulent field, k is the wavenumber and the spectral exponent $\beta = 1 + 2H$, hence the famous "5/3 law".

If we apply the Kolmogorov law to the atmosphere, we must understand and account for the gravity-induced stratification. In the classical quasi-geostrophic approach (Charney, 1971), this is handled by considering the stratification to occur at the very largest scales which are modeled by (quasi flat) horizontal isotropic (2D) turbulence with the smallest scales being isotropic in three dimensions. However gravity acts at all scales, not only the largest and empirical evidence points towards a spatially anisotropic scaling atmosphere (see the reviews (Lovejoy and Schertzer, 2010, 2013)). In the 23/9D model (Schertzer and Lovejoy, 1985b), the turbulence is never isotropic so that (even ignoring intermittency) the classical (isotropic) Kolmogorov law never holds. Nevertheless, the energy flux governs the horizontal dynamics so that the Kolmogorov exponent is still fundamental for the horizontal statistics, and this from the small dissipation scale (~1 mm) up to the largest, planetary scales. In contrast, in the vertical, the buoyancy variance flux dominates the dynamics so that a different exponent is fundamental, the Bolgiano–Obukhov exponent: $H_v = 3/5$ (ignoring intermittency, $\beta_v = 11/5$; Bolgiano, 1959; Obukhov, 1959). The simultaneous action of the two anisotropic cascades leads to an overall 23/9D turbulence model intermediate between flat (2D) and isotropic (3D) turbulence (Schertzer and Lovejoy, 1985a). This model thus has a single anisotropic scaling regime describing the stratification of turbulent structures in the atmosphere, from millimeters to planetary scales.

This 23/9D model provoked a debate sparked by the reinterpretation of aircraft measurements (Lovejoy et al., 2009a, 2009b, 2009c, 2010; Lindborg et al., 2009, 2010; Schertzer et al., 2011; Yano, 2009; Frehlich and Sharman, 2010) followed by the massive (Pinel et al., 2012) re-evaluation of commercial aircraft measurements, and the derivation (Schertzer et al., 2012) of fractional vorticity equations respecting anisotropic scaling symmetries. The latter provide respectively empirical and theoretical arguments in favor of the 23/9D model that are difficult to refute. This raises the question: if the spatial structures do indeed respect anisotropic scaling, what are the implications for the temporal evolution, i.e. the full space–time scaling? Since (x, y, z, t) data sets spanning significant ranges of scales are not available we consider the simpler problem: what are the horizontal–temporal statistics?

Although our goal is to understand Eulerian (fixed frame) statistics, first recall that a general feature of turbulent flows is that there exists a statistical relation between the shears of structures and their lifetimes (their "eddy turnover time"); for Kolmogorov turbulence this is $\Delta v = \varepsilon^{1/2} \Delta t^{H_\tau}$ with $H_\tau = 1/2$, a Lagrangian relation which is used conceptually in meteorology in constructing space–time "Stommel" diagrams (see e.g. Dias et al., 2012). In this paper, instead we estimate the corresponding Eulerian space–time relationships. A classical way to obtain Eulerian statistics is to consider the case when the turbulent fluctuations are sufficiently small compared to an imposed mean flow, such that a clear scale separation exists. Taylor's hypothesis of "frozen turbulence" developed for wind tunnels experiments (Taylor, 1938) can then be used. In this case, a constant (mean flow) velocity V relates temporal to spatial statistics so that $\Delta v = \varepsilon^{1/3} (V \Delta t)^{1/3}$so that $H_\tau = 1/3$ (or β_τ =5/3). However, in the atmosphere, we have argued that no scale separation exists so that another model for space–time scaling is needed.

Without a scale separation, Tennekes (1975) argued that in the Eulerian framework, the turbulent eddies would "sweep" the small eddies. Since the velocity difference across an eddy is $\sim \Delta v \sim \varepsilon^{1/3} \Delta x^{1/3}$, the largest eddies with largest velocities V_e would dominate so that at a fixed location, for time interval Δt, we would have $\Delta v \sim \varepsilon^{1/3} (V_e \Delta t)^{1/3}$ and thus $H_\tau = 1/3$ so that the Eulerian exponent would be different from the Lagrangian one. Radkevich et al. (2008) found empirical support for this by analyzing passive scalar concentrations in the atmosphere (using lidar backscatter as a surrogate), finding values of H_τ mostly $\approx 1/3$ but occasionally $\approx 1/2$. It was argued that the latter values were consequences of the vertical wind dominating the statistics, not a manifestation of the Lagrangian exponent (Lovejoy et al., 2008).

Unfortunately, full (3D) space–time data with wide ranges of scale are not available and reanalyses have limitations, including the use of the hydrostatic approximation (see Stolle et al., 2010; Stolle et al., 2012). Therefore, to better understand the horizontal Eulerian statistics, we present a spectral study of the space–time scaling of atmospheric variability and its (horizontal) space–time statistical relations, using infrared radiances measured by the geostationary multi-functional transport satellite (MTSAT). These infrared radiances are probably the best data currently available for this task as they cover wide scale ranges in both space and time (5 km to ~10000 km, 1 h to months, years). For scenes extracted not too far from the equator, the map projections are straightforward. Here, they do not lead to significant spectral distortions (see the appendix in Lovejoy and Schertzer, 2011). The use of either passive thermal emission bands or active sensing is necessary to avoid strong diurnal effects. However, planetary scale active sensors (satellite-borne radars and lidars) have low temporal resolutions with return times of days. We therefore primarily consider thermal IR from a geostationary satellite which is the best available for the purpose (MTSAT). However, we also analyzed infrared and passive microwave radiances measured by the tropical rainfall measuring mission (TRMM) satellite whose sampling protocol is not ideal for temporal analysis but still allows us to investigate the intermittency.

We should make it clear from the outset that the satellite radiances are not considered as surrogates for cloud liquid water content or any other field. Instead, we use turbulence theory and scaling arguments to derive the corresponding space–time radiance statistics directly (including their space–time spectra). This theoretical form is then empirically tested.

Since our geostationary data is (of necessity) centered at the equator and the sector we analyzed (30°S to 40°N) was largely tropical in character, we will say a few words about the classical (deterministic) dynamical meteorology approach to the tropics. Dynamical meteorology starts with a scale analysis of the governing equations, which is quite different from a scaling analysis (see below), attempting to identify terms which are dominant over a given scale range (usually the so-called synoptic scales). It then considers various idealized flows governed by these dominant terms (e.g. wave motions usually obtained by various linearizations). In this framework the main difference between the tropics and the midlatitudes is the relative lack of Coriolis forces in the former contrasting with the classical geostrophic balance with pressure gradient forces in midlatitudes.

In the tropics, the dynamical meteorology picture is that large-scale atmospheric motions are dominated in the zonal direction by the Walker circulation. The latter is produced by the uneven distribution of heating processes over the ocean and land (Walker and Bliss, 1930, 1932, 1937; Bjerknes, 1969), and is associated with the trade winds in the Inter-Tropical Convergence zone. This large scale motion is in turn affected by wave/oscillation-like disturbances at different scales. At interannual scales, the El-Nino-Southern Oscillation phenomenon plays a major role (Neelin et al., 1998; Sarachik and Cane, 2010) whereas at somewhat smaller temporal scales, tropical variability is determined by the Madden–Julian oscillation (Madden and Julian, 1971, 1972, 1994) and equatorial waves (Matsuno, 1966; Wheeler and Kiladis, 1999). The former is a cyclic pattern associated with winds and surface pressure propagating in the eastward direction with a period of 30–60 days whereas the equatorial waves – of some relevance to the high frequency analysis below (1 h to 14 days) – propagate along the equator, with periods typically of a few days. Equatorial waves are often obtained by linearizing the shallow-water equations (Matsuno, 1966). In the meridional direction, the motion of the atmosphere between the equator and roughly latitudes ±30° is described by a Hadley cell; in midlatitudes, where the Coriolis force is important, it involves the "Ferrel cell" (Chamberlain and Hunten, 1987; Cushman-Roisin, 1994).

Although distinguishing midlatitude and tropical phenomenology may have its uses, global scale general circulation models use the same equations to model both the tropics and midlatitudes, i.e. not performing any simplification of the equations according to the aforementioned scale analysis. This convergence of midlatitude and tropical dynamical approaches is also a strength of the stochastic framework we develop below. Indeed, studies of the basic spatial turbulence characteristics of state variables (zonal, meridional winds, vertical velocities, geopotential heights, humidity, temperature) from reanalyses (Lovejoy and Schertzer, 2011) show that the main differences between midlatitude and tropical statistics are also quantitative (primarily the somewhat smaller effective outer scale in the tropics). This can be understood with the help of scaling analyses of the governing equations and the derived fractional vorticity equations (Schertzer et al., 2011). Unlike the scale analysis discussed above which generates simplified equations, each approximately valid over fairly narrow scale ranges, scaling analysis yields equations with anisotropic scaling laws, (e.g. different scaling for the horizontal and vertical directions) each holding over wide scale ranges. In this framework the main difference between the midlatitudes and tropics is only the importance and orientation of the difference between the absolute and relative vorticities, in the local reference frame, therefore only quantitative, not qualitative differences.

In certain respects, our analysis follows the highly cited Wheeler and Kiladis (1999), "WK" approach (see also Hendon and Wheeler, 2008). WK also used space–time spectral analysis of infra red satellite data over much the same latitudes. Their goal was to empirically detect the various equatorial waves predicted by linear theory including the verification of the predicted dispersion relations. However, there are several important differences between the present and WK approaches. To start with, their data were from two years of polar orbiting satellites with 24 hour temporal resolution whereas we use geostationary satellite data at hourly resolutions over about two months i.e. roughly the same scale ratio but with resolutions a factor 24 smaller. This difference precludes us from observing the lower frequency waves. However, probably the most important difference is in our respective treatments of turbulence which strongly dominates the spectrum. The WK approach considers that turbulence contributes an annoying "background" that they remove by an ad hoc averaging and smoothing procedure, in an attempt to obtain a pure wave spectrum. In this paper, we take quite the opposite approach and consider the turbulent part of the spectrum as our object of study and explicitly attempt to theoretically characterize it, testing our observations against the satellite data. To a first approximation, we find that the wave contribution to the spectrum is such a small residual that it may be neglected. Since the theoretical characterization of the turbulent part turns out to be quite accurate, in a refined analysis, it can used to estimate the wavelike part. This is discussed in ~~a~~ separate publication (Pinel and Lovejoy, 2013, 2014) where we argue that the waves themselves are best understood as strongly nonlinear (high Reynold's number) phenomena with nonclassical effective fractional propagators and with dispersion relations constrained primarily by scaling symmetries.

This paper is part of the Ph.D. thesis (Pinel, 2013). One of the figures (Fig. 4) contains a part (the lower right) that has been adapted from the review paper (Lovejoy and Schertzer, 2010), all the other empirical results are new. While the latter paper contains some theoretical developments the full development including the key analysis of subspaces (most of Section 2.2) is presented here for the first time.

On the theoretical side, we use a concrete anisotropic scaling model based on multiplicative cascades (see below) to interpret the results. Section 2 presents a review of the model. In Section 3, we present the results of the spectral study made on MTSAT IR data. Section 4 presents an application of our method in understanding the atmospheric motion vectors which are used to estimate the wind. In addition to the spectral analysis, we also present a more detailed investigation of the scaling behavior of the atmosphere and its space–time statistical relations by examining its intermittency (Section 5).

2. Review and development of the anisotropic scaling model

2.1. Anisotropic scaling in real space

If the turbulent field I has anisotropic space–time scaling, then for each space–time direction:

$$\begin{aligned} \Delta I(\Delta x) &= \varphi_h \ \Delta x^{H_h} \\ \Delta I(\Delta y) &= \varphi_h \ \Delta y^{H_h} \\ \Delta I(\Delta y) &= \varphi_v \ \Delta y^{H_v} \\ \Delta I(\Delta t) &= \varphi_\tau \ \Delta t^{H_\tau} \end{aligned} \tag{1}$$

where ΔI is a fluctuation in a turbulent field I (e.g. $\Delta I(\Delta x) = |I(x + \Delta x) - I(x)|$), φ's are scale by scale conserved turbulent fluxes, Δx, Δy Δz, Δt are the spatial temporal scales over which ΔI is estimated and H is the "non conservation"

Please cite this article as: Pinel, J., et al., The horizontal space–time scaling and cascade structure of the atmosphere and satellite radiances, Atmos. Res. (2014), http://dx.doi.org/10.1016/j.atmosres.2013.11.022

or "mean fluctuation" exponent. As in the case of the horizontal velocity, Eq. (1) assumes unique horizontal, vertical and temporal exponents H_h, H_v and H_τ. If I is a horizontal wind component, we have already described how arguments from classical turbulence theory and dimensional analysis yield for isotropic 3D turbulence: $\varphi_h = \varepsilon^{1/3}$, $H_h = 1/3$ and $\varphi_\tau = \varepsilon^{1/2}$, $H_\tau = 1/2$. Schertzer and Lovejoy (1985a) proposed that in the vertical, the scaling exponent $H_v = 3/5$ on the assumption that a different quadratic invariant- the buoyancy variance flux ϕ ($\varphi_v = \phi^{1/5}$) -dominated the dynamics; see Lovejoy et al. (2007) for empirical confirmation using drop sondes. This value is a consequence of the dimensional analyses proposed by Bolgiano (1959) and Obukhov (1959) for isotropic buoyancy forced turbulence. Analogous laws for passive scalar concentrations ρ can be obtained by making the following change: $\varepsilon \to \chi^{3/2}\varepsilon^{-1/2}$ where χ is the passive scalar variance flux.

The way to combine these laws for any space–time vector displacements is described in Schertzer and Lovejoy (1985b) and Marsan et al. (1996), Schertzer and Lovejoy 2011, using the formalism of "generalized scale invariance". It consists in replacing the usual vector norm for the space–time increments by a different measure of scale – the scale function $[\![\underline{\Delta R}]\!]$ – that takes into account the anisotropy. A simple example of such a "canonical" scale function is:

$$\Delta I(\underline{\Delta R}) = \varphi_{h,[\![\underline{\Delta R}]\!]}[\![\underline{\Delta R}]\!]^{H_h};$$

$$[\![\underline{\Delta R}]\!] = L_w\left\{\left(\frac{\Delta x}{L_w}\right)^2 + \left(\frac{\Delta y}{L_w}\right)^2 + \lambda_s^{2(1/H_z-1)}\left(\frac{\Delta z}{L_w}\right)^{2/H_z} + \left(\frac{\Delta t}{\tau_w}\right)^{2/H_t}\right\}^{1/2} \tag{2}$$

where $\underline{\Delta R} = (\underline{\Delta r}, \Delta t)$ with $\underline{\Delta r} = (\Delta x, \Delta y, \Delta z)$; L_w is a convenient reference scale (see below), of the order of the size of the Earth ($L_e = 20000$ km) and $\tau_w = \varepsilon^{-1/3}L_w^{2/3}$ is the corresponding duration, the lifetime of planetary scale structures; the subscript "w" is for "weather". $\varphi_{h,[\![\underline{\Delta R}]\!]}$ is the turbulent flux governing the dynamics in the horizontal at resolution $[\![\underline{\Delta R}]\!]$ and $\lambda_s = L_w/l_s$ where $l_s = \phi^{-3/4}\varepsilon^{5/4}$ is the "sphero-scale" (i.e. the scale at which structures are roughly roundish i.e. $[\![l_s,0,0,\Delta t]\!] = [\![0,l_s,0,\Delta t]\!] = [\![0,0,l_s,\Delta t]\!]$. Here we introduced the exponents $H_z = H_h/H_v$ and $H_t = H_h/H_\tau$ that characterize the vertical–horizontal and (horizontal) space–time stratifications. For the wind and passive scalars, $H_h = 1/3, H_v = 3/5, H_\tau = 1/2$, $H_z = 5/9$, and $H_t = 2/3$. The use of the temporal Lagrangian exponent in the above Eulerian Eq. (2) is valid when there is no mean advection. Note that when $\underline{\Delta R}$ is aligned with one of the axes in our coordinate system, (e.g. $\underline{\Delta R} = (\Delta x, 0, 0, 0)$), we retrieve Eq. (1) for that particular direction. Finally, the vertical extent of structures of horizontal size L is L^{H_z}; their volumes are $L^{D_{el}}$ with $D_{el} = 2 + H_z = 23/9$; this is the 23/9D model (Schertzer and Lovejoy, 1985a, 1985b).

Using the scale function, taking the qth order moments and averaging, the statistics of the space–time fluctuation $\Delta I(\underline{\Delta R})$ follow the qth order structure function:

$$S_q(\underline{\Delta R}) = \langle|\Delta I(\underline{\Delta R})|^q\rangle = \left\langle\varphi^q_{[\![\underline{\Delta R}]\!]}\right\rangle [\![\underline{\Delta R}]\!]^{qH_h} \propto [\![\underline{\Delta R}]\!]^{\xi(q)}; \tag{3}$$

$$\left\langle\varphi^q_{[\![\underline{\Delta R}]\!]}\right\rangle \propto \left(\frac{L_w}{[\![\underline{\Delta R}]\!]}\right)^{K(q)}; \qquad \xi(q) = qH - K(q)$$

where the function $K(q)$ takes into account the intermittency of the flux φ and yields the structure function exponent $\xi(q)$ as indicated. Its statistical behavior is determined by multiplicative cascades whose external scale is L_w and which we discuss in Section 5.

The scale function (Eq. (2)) uses only the Lagrangian temporal scaling; it ignores advection. In the Eulerian frame, we also need to take into account the mean advection of structures. For a fixed advection velocity $\underline{v} = (v_x, v_y, v_z)$, we can use the Gallilean transformation $\underline{r} \to \underline{r}–\underline{v}t$; $t \to t$, to obtain:

$$[\![\underline{\Delta R}]\!]_{advec} = L_w\left\{\left(\frac{\Delta x - v_x\Delta t}{L_w}\right)^2 + \left(\frac{\Delta y - v_y\Delta t}{(L_w/a)}\right)^2 + \lambda_s^{2(1/H_z-1)}\left(\frac{\Delta z - v_z\Delta t}{L_w}\right)^{2/H_z} + \left(\frac{\Delta t}{\tau_w}\right)^{2/H_t}\right\}^{1/2} \tag{4}$$

where we also introduced a, a parameter that describes the possible trivial (scale independent) zonal/meridional anisotropy in the horizontal spatial plane.

The basic problem now is that Eq. (4) holds only for a fixed, constant and uniform advection $\underline{v}$ whereas the actual advecting $\underline{v}$ is a turbulent field, i.e. we must consider an "effective" scale function that takes into account the turbulent nature of $\underline{v}$. The situation is complicated by the fact that at fixed location (i.e. $\Delta x = \Delta y = \Delta z = 0$), there are four temporal terms and each can in principle be dominant depending on the $\underline{v}$ field. In Lovejoy et al. (2008) and Radkevich et al. (2008), it was argued that sometimes the vertical wind term (the 3rd on the right in Eq. (4)) can dominate the statistics of the horizontal wind, producing $\Delta v \approx \Delta t^H$ with $H \approx 0.5$ scaling. To see how this might arise, take $\Delta z = 0$, so that the vertical term in Eq. (4) is $\propto(v_z\Delta t)^{1/H_z}$. Unlike the horizontal wind, the vertical wind has typically small values and follows $|v_z| \propto \Delta t^{H_{v_z}}$ with empirically $H_{v_z} \approx -0.2$ (see Lovejoy and Schertzer, 2011). From Eq. (4), taking $H_z = 5/9$ and neglecting the intermittency, we find: the effective scale function at zero spatial lag is $\propto\Delta t^{(H_{v_z}+1)/H_z} = \Delta t^{1/H}$[illegible] with $H_{\tau,eff}$ [illegible]0.7 ~ $H_t = 2/3$; hence taking the H~~subscript~~[illegible]/3 power (eq. 3) we obtain $\Delta v \sim \Delta t^{0.5}$ scaling when this vertical term is dominant (corresponding to the spectrum $E(\omega) \sim \omega^{-2}$). In the following, we consider only satellite radiance fields, which are (x, y, t) fields. The consequence of the vertical wind on the radiances is therefore quite different. Since our field is horizontal, we take $\underline{\Delta R} = (\underline{\Delta r}, \Delta t)$ where $\underline{\Delta r} = (\Delta x, \Delta y)$, so that for constant advection $\underline{v} = (v_x, v_y)$, (i.e. $v_z = 0$ in Eq. (4)) we have:

$$[\![\underline{\Delta R}]\!]_{advec,hor} = L_w\left\{\left(\frac{\Delta x - v_x\Delta t}{L_w}\right)^2 + \left(\frac{\Delta y - v_y\Delta t}{L_w/a}\right)^2 + \left(\frac{\Delta t}{\tau_w}\right)^{2/H_t}\right\}^{1/2}. \tag{5}$$

We have mentioned that the largest eddies with speed $V_w = L_w/\tau_w$ advect all the others so that the "effective" Eulerian scale function will involve averages over v's ranging up to V_w. Using this in Eq. (5) for v_x and ignoring v_y, we see that whenever $\Delta t < \tau_w$, the corresponding advection term $\left|\frac{\Delta t}{\tau_w}\right|^{1/H_t} = \left|\frac{\Delta t}{\tau_w}\right|^{3/2}$ will dominate the temporal scaling term $\left|\frac{V_w\Delta t}{L_w}\right| = \left|\frac{\Delta t}{\tau_w}\right|$. Indeed, as argued in Radkevich et al. (2007) using meteorological analyses from a component of the operational Canadian Meteorological Centre Global Environmental Multiscale (GEM) model, the empirical probability that the transition scale – from horizontal advection scaling to pure time evolution scaling – is shorter than τ_w (~10 days) is low, hence we drop the Lagrangian term.

Please cite this article as: Pinel, J., et al., The horizontal space–time scaling and cascade structure of the atmosphere and satellite radiances, Atmos. Res. (2014), http://dx.doi.org/10.1016/j.atmosres.2013.11.022

Considering only the first two terms on the right hand side of Eq. (5), there will be two main effects of turbulence that we must consider. The first is the advection by the mean $\underline{v}$, the second is the effect of the turbulent variability which is conveniently estimated by its variance. The two effects can conveniently be understood by considering the square of the scale function:

$$\begin{aligned}[\![\underline{\Delta R}]\!]^2_{advec,hor} &= L_w^2\left\{\left(\frac{\Delta x - v_x\Delta t}{L_w}\right)^2 + \left(\frac{\Delta y - v_y\Delta t}{(L_w/a)}\right)^2\right\}\\ &= L_w^2\left\{\left(\frac{\Delta x}{L_w}\right)^2 + \left(\frac{a\Delta y}{L_w}\right)^2 + \left(\frac{{v_x}^2 + a^2{v_y}^2}{L_w^2}\right)\Delta t^2 - 2\left(\frac{v_x\Delta x}{L_w} + \frac{a^2 v_y\Delta y}{L_w}\right)\left(\frac{\Delta t}{L_w}\right)\right\}.\end{aligned} \tag{6}$$

We can now approximately take into account the effects of turbulence by averaging both sides of Eq. (6) over a turbulent $\underline{v}$ field. Doing this, we obtain:

$$[\![\underline{\Delta R}]\!]^2 = \underline{\Delta R}^T\underline{\underline{B}}\,\underline{\Delta R} \tag{7}$$

where $[\![\underline{\Delta R}]\!]$ is the "effective" scale function obtained by averaging, "T" indicates transpose, and $\underline{\Delta R} = (\Delta x, \Delta y, \Delta t)$ and

$$\underline{\underline{B}} = \begin{pmatrix} 1 & 0 & -\mu_x \\ 0 & a^2 & -a^2 y \\ -\mu_x & -a^2\mu_y & 1 \end{pmatrix} \tag{8}$$

where we have used the following transformation to nondimensionalize the parameters:

$$\Delta x \to \frac{\Delta x}{L_w};\quad \Delta y \to \frac{a\Delta y}{L_w};\quad \Delta t \to \frac{\Delta t}{\tau_w};\quad \mu_x = \frac{\overline{v_y}}{V_w};\quad \underline{\mu} = \left(\mu_x, \mu_y\right) \tag{9}$$

and $\underline{\overline{v}} = \left(\overline{v}_x, \overline{v}_y\right)$ and $V_w = \left(\overline{v_x^2} + a^2\overline{v_y^2}\right)^{1/2}$ where $\underline{\overline{v}}$ is the overall mean advection in the region studied and V_w is a large-scale turbulent velocity; $\overline{v^2}$ is the mean square. Note that since $\overline{v^2} > (\overline{v})^2$, $|\mu_x| < 1$. These results are generalizations of those presented in Lovejoy and Schertzer (2010), who considered $a = 1$~~)~~.

2.2. Anisotropic scaling in Fourier space

If the increments in a turbulent field I are described by the scaling in Eq. (3), then, we expect the spectral density $P(\underline{K})$ to be scaling as well, but with a different (Fourier space) scale function $[\![\underline{K}]\!]_F$ where $\underline{K} = (k_x, k_y, \omega)$, the k's being the wavenumbers in the horizontal plane and ω the frequency. To derive this, we start from the general relation between second order structure functions and spectra (a corollary of the Wiener–Khintchin theorem):

$$\left\langle |\Delta I(\underline{\Delta R})|^2\right\rangle = 2\int d\underline{K}\ \left(1 - e^{i\underline{K}\cdot\underline{\Delta R}}\right)\ P(\underline{K}) \tag{10}$$

In order to determine the form of $P(\underline{K})$, we define the dimensionless wave vector: $\underline{K} \to \left(L_w k_x, L_w k_y, \tau_w\omega\right)$ and use the relation:

$$|\underline{\Delta R}|^{\zeta(2)} = 2\int |\underline{K}|^{-(D+\zeta(2))}\left(1 - e^{i\underline{K}\cdot\underline{\Delta R}}\right)d\underline{K} \tag{11}$$

where |.| is the usual vector norm. Eqs. (10) and (11) state that, if the integral converges and the (isotropic) spectral density obeys a scaling behavior (i.e. $P(\underline{K}) \sim |\underline{K}|^{-s}$), then $|\underline{\Delta R}|$ is scaling as well and their scaling exponents are related by $s = \xi(2) + d$ (with $d = 3$). For real fields, the scaling is always only valid for a finite range of scales and the corresponding truncated integral always converges. If we make the change of variable $\underline{K} \to \underline{\underline{C}}^{-1}\underline{K}$, (with $\underline{\underline{C}}^{-1}$ a real matrix), we obtain:

$$\left\langle |\Delta I(\underline{\Delta R})|^2\right\rangle \approx [\![\underline{\Delta R}]\!]^{\xi(2)} \leftrightarrow P(\underline{K}) \propto \left\langle\left|\tilde{I}(\underline{K})\right|^2\right\rangle \approx [\![\underline{K}]\!]_F^{-s};\quad s = \xi\ (2) + 3 \tag{12}$$

$$[\![\underline{\Delta R}]\!] = \left(\underline{\Delta R}^T\underline{\underline{B}}\,\underline{\Delta R}\right)^{1/2} \leftrightarrow [\![\underline{K}]\!]_F = \left(\underline{K}^T\underline{\underline{B}}^{-1}\underline{K}\right)^{1/2};\qquad \underline{\underline{B}} = \underline{\underline{C}}\,\underline{\underline{C}}^T$$

with:

$$\underline{\underline{B}}^{-1} = \frac{1}{1 - \mu_x^2 - a^2\mu_y^2}\begin{pmatrix} 1 - a^2\mu_y^2 & \mu_x\mu_y & \mu_x \\ \mu_x\mu_y & \left(1 - \mu_x^2\right)/a^2 & \mu_y \\ \mu_x & \mu_y & 1 \end{pmatrix} \tag{13}$$

from Eq. (8). Since $\det\left(\underline{\underline{C}}\,\underline{\underline{C}}^T\right) = \left(\det\underline{\underline{C}}\right)^2 = \det\underline{\underline{B}}$ and $\underline{\underline{C}}$ is real we have $\det\underline{\underline{B}} > 0$ so that the result for $\det\left(\underline{\underline{B}}\right) < 0$ cannot be obtained from this approach and has qualitatively different wave behavior (see Lovejoy and Schertzer, 2013; Pinel and Lovejoy, 2013, 2014). Alternatively, note that since $\det\left(\underline{\underline{B}}\right) = a^2\left(1 - \mu_x^2 - a^2\mu_y^2\right)$, $\det\left(\underline{\underline{B}}\right) > 0$ when $\mu_x^2 + a^2\mu_y^2 < 1$, a condition which is always satisfied. Notice that we introduced the exponent $\xi(2)$ in Eq. (11) that takes into account the non-conservation exponent H as well as the second order intermittency correction (see below).

We can further simplify the form of $[\![\underline{K}]\!]_F$ by introducing:

$$\mu_x' = \frac{\mu_x}{\left\{1 - \left(\mu_x^2 + a^2\mu_y^2\right)\right\}};\qquad \mu_y' = \frac{\mu_y}{\left\{1 - \left(\mu_x^2 + a^2\mu_y^2\right)\right\}}; \tag{14}$$

$$\omega' = \frac{\omega}{\left\{1 - \left(\mu_x^2 + a^2\mu_y^2\right)\right\}}$$

to obtain:

$$[\![\underline{K}]\!]_F = \left(\underline{K}^T\underline{\underline{B}}^{-\cancel{2}}\underline{K}\right)^{1/2} = \left\{\left(\omega' + \underline{k}\cdot\underline{\mu}'\right)^2 + \|\underline{k}\|^2\right\}^{1/2};\qquad \|\underline{k}\|^2 = k_x^2 + \left(k_y/a\right)^2 \tag{15}$$

and the final expression for the spectral density:

$$P(\underline{K}) \approx P_0[\![\underline{K}]\!]_F^{-s} = P_0\left\{\left(\omega' + \underline{k}\cdot\underline{\mu}'\right)^2 + \|\underline{k}\|^2\right\}^{-s/2} \tag{16}$$

where P_0 is a dimensional constant and $\|\underline{k}\|^2$ is a spatial Fourier scale function. Note that we can express the parameters: $\mu_x' = \frac{\overline{v_x}}{\sigma_v}$; $\mu_y' = \frac{\overline{v_y}}{\sigma_v}$ with $\sigma_v^2 = \left(\overline{v_x^2} - \overline{v_x}^2\right) - a^2\left(\overline{v_y^2} - \overline{v_y}^2\right)$ so that $\frac{\mu_x'}{\mu_x} = \frac{\mu_y'}{\mu_y} = \frac{V_e}{\sigma_v}$; the parameter $\underline{\mu}'$ thus being directly related to the mean advection.

Directly testing the prediction that the horizontal space–time spectral density is of the form of Eq. (12) is unwieldy; it is more convenient to consider various 2D and 1D subspaces, obtained by successively integrating out k_x, k_y, ω in $P(\underline{K}) = P_{xyt}(k_x, k_y, \omega)$. To do this, we use the Wiener–Khintchin

Please cite this article as: Pinel, J., et al., The horizontal space–time scaling and cascade structure of the atmosphere and satellite radiances, Atmos. Res. (2014), http://dx.doi.org/10.1016/j.atmosres.2013.11.022

theorem that relates the autocorrelation function to the spectral density:

$$R(\Delta x, \Delta y, \Delta t) = (2\pi)^{-3} \int P_{xyt}\left(k_x,\ k_y,\ \omega\right)\ e^{i\left(k_x \Delta x + k_y \Delta y + \omega \Delta t\right)} dk_x dk_y d\omega. \tag{17}$$

If we successively put $\Delta t = 0$, $\Delta y = 0$, and $\Delta x = 0$, we obtain:

$$\begin{aligned}
&R(\Delta x, \Delta y, 0) = (2\pi)^{-2} \int P_{xy}\left(k_x,\ k_y\right)\ e^{i\left(k_x \Delta x + k_y \Delta y\right)} dk_x dk_y;\\
&P_{xy}\left(k_x,\ k_y\right) = \int P\left(k_x,\ k_y,\ \omega\right)\ d\omega\\
&R(\Delta x, 0, \Delta t) = (2\pi)^{-2} \int P_{xt}(k_x,\ \omega)\ e^{i\left(k_x \Delta x + \omega \Delta t\right)} dk_x d\omega;\\
&P_{xt}(k_x,\ \omega) = \int P\left(k_x,\ k_y,\ \omega\right)\ dk_y\\
&R(0, \Delta y, \Delta t) = (2\pi)^{-2} \int P_{yt}\left(k_y,\ \omega\right)\ e^{i\left(k_y \Delta y + \omega \Delta t\right)} dk_y d\omega;\\
&P_{yt}\left(k_y,\ \omega\right) = \int P\left(k_x,\ k_y,\ \omega\right)\ dk_x.
\end{aligned} \tag{18}$$

From Eq. (18) and developments similar to Eqs. (11)–(13), we define:

$$\begin{aligned}
&P_{xy}\left(k_x,\ k_y\right) = \left\|\left(k_x,\ k_y\right)\right\|_{xy}^{-(s-1)};\\
&P_{xt}(k_x,\ \omega) = \left\|(k_x,\ \omega)\right\|_{xt}^{-(s-1)}\\
&P_{yt}\left(k_y,\ \omega\right) = \left\|\left(k_y,\ \omega\right)\right\|_{yt}^{-(s-1)}
\end{aligned} \tag{19}$$

and we find:

$$\begin{aligned}
&\left\|\left(k_x,\ k_y\right)\right\|_{xy}^2 = k_x^2 + a^{-2} k_y^2\\
&\left\|(k_x,\ \omega)\right\|_{xt}^2 = \left(\omega_x' + k_x \mu''_x\right)^2 + k_x^2;\\
&\mu''_x = \frac{\overline{v_x}}{\left(\sigma_v^2 + a^2\left(\overline{v_y}\right)^2\right)^{1/2}} = \frac{\mu_x'}{\left(1 + a^2 \mu_y'^{\,2}\right)^{1/2}};\\
&\omega_x' = \frac{\omega}{\left(1 - \mu_x^2\right)^{1/2}}\\
&\left\|\left(k_y,\ \omega\right)\right\|_{yt}^2 = \left(\omega_y' + k_y \mu''_y\right)^2 + k_y^2;\\
&\mu''_y = \frac{\overline{v_y}}{\left(\sigma_v^2 + \left(\overline{v_x}\right)^2\right)^{1/2}} = \frac{\mu_y'}{\left(1 + \mu_x'^{\,2}\right)^{1/2}}; \qquad \omega_y' = \frac{\omega}{\left(1 - a^2 \mu_y^2\right)^{1/2}}.
\end{aligned} \tag{20}$$

Similarly, for the 1D subspaces, we obtain:

$$\begin{aligned}
&E_x(k_x) = \int P\left(k_x,\ k_y,\ \omega\right)\ d\omega\ dk_y \sim k_x^{-\beta}; \qquad \beta = s - 2\\
&E_y\left(k_y\right) = \int P\left(k_x,\ k_y,\ \omega\right)\ d\omega\ dk_x \sim k_y^{-\beta}\\
&E_t(\omega) = \int P\left(k_x,\ k_y,\ \omega\right)\ dk_x\ dk_y \sim \omega^{-\beta}.
\end{aligned} \tag{21}$$

3. MTSAT IR data analysis

3.1. MTSAT data

We now test the spectrum Eq. (16) with infrared radiance data measured by the MTSAT satellites which are a series of geostationary weather satellites operated by the Japan Meteorological Agency. MTSAT-1R, the first of the series, was launched in 2005 and replaced the older series of Geostationary Meteorological Satellites (GMS, also called "Himawari", operational since 1977). It measures radiances from the region centered on longitude 140° East (Japan, tropical western Pacific, Australia) over five channels: one visible (0.55–0.90 μm), four infrared (10.3–11.3 μm; 11.5–12.5 μm; 6.5–7.0 μm and 3.5–4.0 μm). MTSAT-1R has a maximal resolution of 1 km (visible) and 4 km (infrared) at nadir. The temporal resolution is 30 min (above the equator) and 1 h (full disk), (Takeuchi et al., 2010; Puschell et al., 2002, 2003).

We analyzed 1386 images (~two months of data, September and October 2007), from the first ("thermal") infrared channel (10.3–11.3 μm, sensitive to temperature at (roughly) the top of clouds) taken from the Atmospheric Radiation Measurement database that archives MTSAT-1R data at 5 km and 1 hour resolutions over latitudes 40°S–30°N and longitudes 80°E–200°E (a Mercator projection was used; see Fig. 1). This corresponds to 1675 × 2672 pixel images (north–south, east–west) covering a region 8375 by 13 360 km.

3.2. MTSAT spectra

We separated the MTSAT sample into five 277 h (~12 day) blocks (with resolutions, 30 km, 1 h), calculating for each block (of 277 h by ~8000 km (N–S) by ~13 000 km (E–W)), the spectral density of fluctuations of the field with respect to the mean image (over the 2 month period); in addition, we used a standard Hann window to reduce spectral leakage. Due to the land and ocean surfaces as well as clouds, the images are variable in space and in time, however, it is the clouds that dominate the variability over the scales considered here. After averaging over the five time blocks to improve the statistics, we compared the results to the theoretical form (Eq. (16)). Figs. 2 and 3 show the comparisons for 1D and 2D subspaces (Eqs. (18)–(21)) between MTSAT data and a regression from Eq. (16). It is convenient to introduce three dimensional parameters P_0, L_w and τ_w even though only two may be determined independently. This means that we may take L_w–$L_\mathrm{e} = 20\,000$ km; τ_w and P_0 are then uniquely determined by the regression with τ_w corresponding to the lifetime of planetary structures (size L_w). The parameters we found are (see also Table 1):

$$\begin{aligned}
&V_\mathrm{w} = 41 \pm 3\ \ \mathrm{km/h} \approx 1000\ \ \mathrm{km/day}; \qquad \tau_\mathrm{w} = L_\mathrm{w}/V_\mathrm{w} \sim 20 \pm 1\ \ \mathrm{days}\ ;\\
&a \sim \quad 1.2 \pm 0.1\ ;\ \ \mathrm{s} \sim 3.4 \pm 0.1\\
&\mu_\mathrm{x} \sim -0.3 \pm 0.1\ ;\ \ (\overline{v}_x \sim\ \ -12 \pm 4\ \ \mathrm{km/h} \approx -300\ \ \mathrm{km/day})\ ;\\
&\mu_\mathrm{y} \sim 0.10 \pm 0.08\ ;\left(\overline{v}_y \sim\ \ 4 \pm 3\ \ \mathrm{km/h} \approx 100\ \ \mathrm{km/day}\right);\\
&\mathrm{P}_0 = 2.8 \pm 0.2^\circ\mathrm{C}^2\mathrm{km}^2\mathrm{h}.
\end{aligned} \tag{22}$$

From Fig. 2, we see that the 1D spectra are very close to power laws over the range of scales 60–5000 km in space and 2–100 h in time (except for expected and relatively small diurnal cycle contributions at 12 and 24 h. cf. (Hsu et al., 2006, 2011)). The exponents are $\beta \sim 1.55 \pm 0.01$, a bit smaller than the non-intermittent passive scalar, Corrsin–Obukhov value $\beta = 5/3$, (with intermittency corrections, the latter are nearly identical, see (Lilley et al., 2008)). We thus have space–time isotropy in the spectral exponents, as predicted (Eq. (21)). However, the scaling is even better than suggested by the near linearity displayed in Fig. 2.

Please cite this article as: Pinel, J., et al., The horizontal space–time scaling and cascade structure of the atmosphere and satellite radiances, Atmos. Res. (2014), http://dx.doi.org/10.1016/j.atmosres.2013.11.022

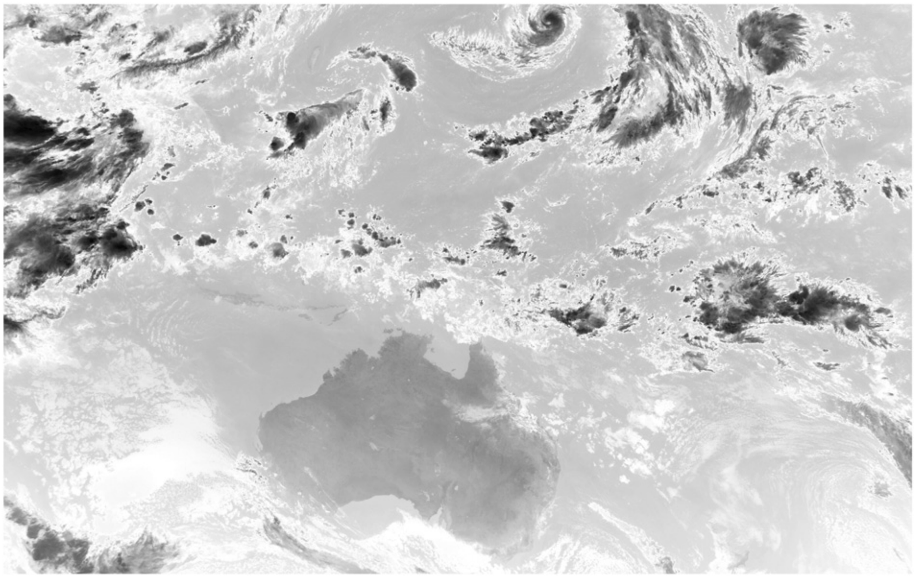

Fig. 1. Thermal IR MTSAT-1R image taken on September 9, 2007, at 5 km resolution; between latitudes 40°S–30°N and longitudes 80°E–200°E. We can easily recognize the shape of Australia at the bottom and observe various cloud structures.

Indeed, we expect deviations from log–log linearity due to the space–time anisotropy coupled with our finite sample size which breaks the scaling symmetry at high and low wavenumbers/frequencies. When the integrals in Eq. (21) are performed on the discretized, numerically integrated theoretical expressions, we see (Fig. 2) that much of the curvature at both ends of the spectra can be explained, although for spatial scales ≥ 6000 km or temporal scales longer than ~100 h, deviations become important. Note that the regression value $V_w = L_w/\tau_w = 41$ km/h is also consistent

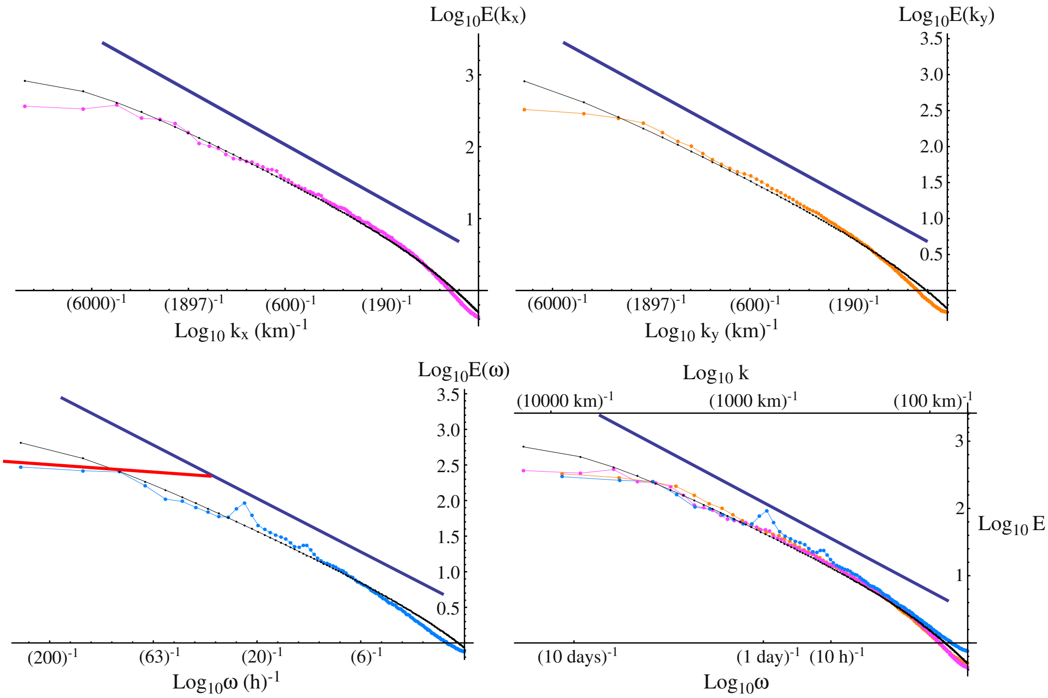

Fig. 2. 1D spectra. In black: the theoretical spectrum using parameters estimated by regression from Eq. (16) and taking into account the finite space–time sampling volume. The parameters are: L_w ~ 20000 km; τ_w ~ 20 ± 1 days; ($V_w \sim L_w/\tau_w = 41$ km/h = 984 km/day); a ~ 1.2 ± 0.1; s ~ 3.4 ± 0.1; μ_x ~ −0.3 ± 0.1; (v_x −12 ± 4 km/h ≈ −295 km/day); μ_y ~ 0.10 ± 0.08; (v_y 4 ± 3 km/h ≈ 98 km/day); $P_0 = 2.8 \pm 0.2$ K^2 km^2 h. In color: MTSAT thermal IR radiances. The straight lines are reference lines with slopes −1.5 (blue) and −0.2 (red). Upper left: zonal spectrum. Upper right: meridional spectrum. Bottom left: temporal spectrum. Bottom right: superposition of zonal, meridional and temporal spectra. (For interpretation of the references to color in this figure legend, the reader is referred to the web version of this article.)

Please cite this article as: Pinel, J., et al., The horizontal space–time scaling and cascade structure of the atmosphere and satellite radiances, Atmos. Res. (2014), http://dx.doi.org/10.1016/j.atmosres.2013.11.022

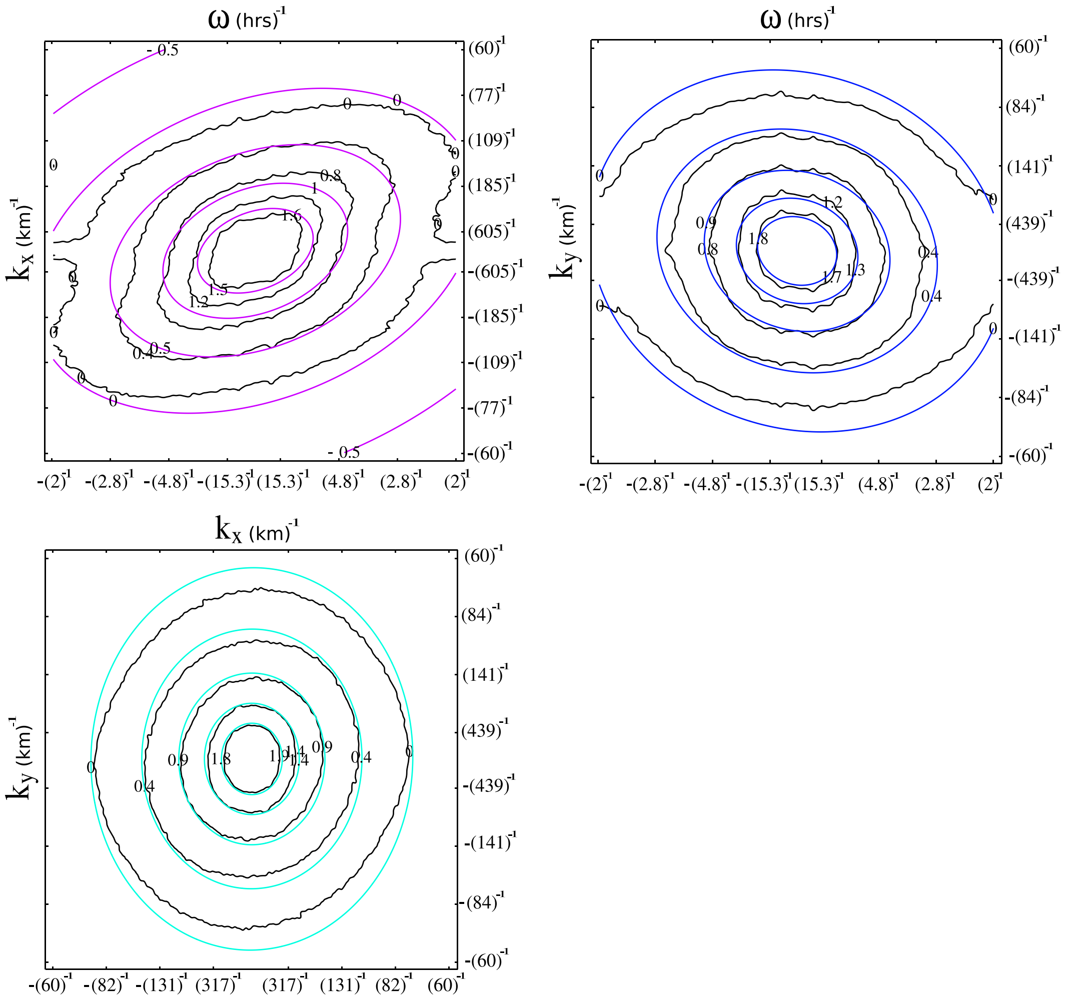

Fig. 3. Contours of log of spectral densities projected on to 2D subspaces. In color: the fit from theoretical expression (Eq. (16)) with parameters: as in fig. 2. In black: MTSAT thermal IR radiances. Upper left: $\text{Log}_{10}P(k_x, \omega)$; zonal wavenumber/frequency subspace. Upper right: $\text{Log}_{10}P(k_y, \omega)$; meridional wavenumber/frequency subspace. Bottom: $\text{Log}_{10}P(k_x, k_y)$; spatial spectral density. (For interpretation of the references to color in this figure legend, the reader is referred to the web version of this article.)

with the values $L_w = 5000$ km and $\tau_w = 120$ h (with $P_0 = 0.03$ °CK^2 km^2 h; the radiances are in units of equivalent black body temperature), which are roughly the scales at which the scaling is broken; these are denoted L_d and τ_d for space and time respectively (Table 1; see Fig. 2 in the north–south direction, $L_d/a \approx 4300$ km).

To understand the break in the temporal spectrum at large scales, fig. 2 shows that as expected there is a statistical relation between the size of structures and their lifetimes. As the scaling symmetry seems to generally hold in space for scales as large as planetary scales (see the review (Lovejoy and Schertzer, 2010)), it was estimated by Lovejoy and Schertzer (2010) from "first principles" (i.e. using the energy flux due to solar radiation) and from ECMWF reanalyses that structures of planetary scale L_e have typical lifetimes of $\tau_e = \varepsilon^{-1/3}L_e^{2/3}$ ~ 10 days. It was also observed that atmospheric fields all undergo a transition in their statistics at a scale $\tau_w \approx \tau_e$, from a small scale regime ($\Delta t < \tau_w$) to a different larger scale regime ($\Delta t > \tau_w$); the two regimes having qualitatively different scaling behaviors with fluctuations growing or decreasing with scale respectively (the sign of H changed from positive to negative at τ_w). It was proposed by Lovejoy and Schertzer (2010, 2012, 2013) to identify the former regime with weather and the latter as "macroweather" this replaces the earlier descriptive term "low frequency weather", see also Lovejoy (2013).

In order to investigate this more fully, we can examine 2D rather than 1D spectra (Eq. (18)). Regressions on the 2D spectra also reproduce the data relatively well, but there are still residuals (see Fig. 3). The mean deviations between the two surfaces (for the three 2D cases shown in Fig. 3) are of the order of ±11% in $\text{Log}_{10}P(k, \omega)$, even though the signal ($P(\underline{K})$) varies over ~five orders of magnitude over the scaling range (60–5000 km in space and 2–100 h in time due to the Nyquist frequency, these are the highest wavenumbers and spectra possible with 30 km, 1 hour data). The orientation of the contours of $\text{Log}_{10}P(k_x, \omega)$ (in zonal wavenumber/frequency subspace) is a consequence of the non zero (and relatively large) mean zonal advection $\overline{v_x}$ ~ -12 ± 4 km/h (-300 km/day). Hence, with our contours, we can estimate the overall mean advection. The area analyzed in this paper is not perfectly

Please cite this article as: Pinel, J., et al., The horizontal space–time scaling and cascade structure of the atmosphere and satellite radiances, Atmos. Res. (2014), http://dx.doi.org/10.1016/j.atmosres.2013.11.022

Table 1
A comparison of different parameters obtained from the spectral method (Section 3) and from statistical moments (Section 5) as well as results from a previous TRMM analysis in the along track direction (Lovejoy et al., 2009d). L_d and τ_d are the (large) spatial and temporal scales respectively beyond which the scaling symmetry breaks down. The speed V provides an estimate of the statistical relation between the size of structures and their lifetimes, i.e. it corresponds to V_w evaluated by the spectral method (Section 3) or an averaged (north–south, east–west) value V_{eff} evaluated from the cascade analysis (Section 5). The parameter a from the spectral method was directly estimated from the regression while for the statistical moments, a is an averaged value from the "shifting method" and from the Eulerian Stommel diagrams (Section 5.3). Generally, values of parameters obtained for MTSAT by spectral and statistical moment methods are comparable. We find small discrepancies between parameters found for MTSAT, VIRS-5 and TMI-8, even though the values of C_1 and a are comparable (except for TMI-8). Interestingly, the values of L_{eff} found in the north–south direction are comparable with those found by (Lovejoy et al., 2009d) in the direction of the orbit.

		Spectra	Statistical moments				
			This study			Lovejoy et al. (2009d)	
		MTSAT	MTSAT	VIRS-5	TMI-8	VIRS-5	TMI-8
Resolutions	Space (km)	30	30	100	100	8.8	13.9
	Time (h)	1	1	24	24	–	–
C_1		–	0.07	0.07	0.05	0.084	0.102
α		–	1.5–1.6	1.8	2	1.63	1.90
L_{eff}	E–W (km)	–	50 000	25 000	12 600	12 600	6300
	N–S (km)	–	32 000	12 600	8000	(orb. dir.)	(orb. dir.)
τ_{eff}	Time (days)	–	48	57	57	–	–
L_d	E–W (km)	5000	6000	12 000	5000	10 000	2500
	N–S (km)	2500	2000	9000	2000	(orb. dir.)	(orb. dir.)
τ_d	Time (days)	4	2	14	4	–	–
V	(km/day)	1000	~800	~340	~120	–	–
a		1.2	~1.35	~1.4	1.1	–	–

symmetric with respect to the equator and our data spanned only two months so that we found a small mean advection in the meridional direction.

The functional form Eq. (16) was derived by assuming that the structures were localized, turbulent like; however, there is a longstanding phenomenology of wavelike disturbances (localized in space but not in space-time) so that we may expect that the residual differences between the empirical and theoretical regression space may be associated largely with waves. This is the basic idea behind the technique developed by Wheeler and Kiladis (1999) who also used IR radiances (although at somewhat larger space–time scales). In order to study the residual spectrum believed to be associated with waves, they factored the spectral density into a "red noise" turbulent background and studied the residual part that they associated with waves. However, instead of using a theoretically motivated characterization of the turbulent background (Eq. (16)), they used an ad hoc averaging technique and estimated the wave part of the spectrum as deviations from this. Examining only the (k_x, ω) subspace, they compared the several classical dispersion relations with the residual spectrum obtained by dividing out the turbulent background. We discuss this small residual for MTSAT data and our anisotropic model in Pinel and Lovejoy, 2013, 2014 and Lovejoy and Schertzer (2013) where it is argued that the waves are on the contrary an emergent phenomenon arising from strongly nonlinear but scaling dynamics.

4. Application to atmospheric motion vectors

As an application of the model, we now show that Eq. (16) gives a theoretical basis for extracting "atmospheric motion vectors" (AMV's) from sequences of IR satellite images (Leese et al., 1970; Szantai and Seze, 2008) which are used to determine cloud (or water vapor) "motion" vectors in near real-time from geostationary satellite data; these are used as surrogates for wind vectors for weather forecasting applications. Although several techniques exist to estimate AMV's, they are all variants of the maximum cross correlation technique which is based on the displacement $\underline{\Delta r}_{\max}$ which yields the maximum cross correlation between successive images. From this, the motion vector: $\underline{v}_{motion}=\frac{\underline{\Delta r}_{\max}}{\Delta t}$ is obtained, where Δt is the time interval between consecutive images.

We now estimate $\underline{\Delta r}_{\max}$ and $\underline{v}_{motion}$ from the structure function: $S_2(\underline{\Delta r})$ (see Eq. (3) for $q=2$). $\underline{\Delta r}_{\max}$ can be found, from the condition on the cross-correlation function:

$$R(\underline{\Delta r}_{\max},\Delta t)=\max_{\underline{\Delta r}}\{R(\underline{\Delta r},\Delta t)\} \tag{23}$$

where

$$R(\underline{\Delta r},\Delta t)=\langle I(x,y,t)I(x+\Delta x,y+\Delta y,t+\Delta t)\rangle.$$

Using $R(\underline{\Delta r},\Delta t)=R(0,0)-\frac{1}{2}S_2(\underline{\Delta r},\Delta t)$, we can derive $\underline{v}_{motion}$ in terms of the matrix $\underline{B}$ as follows. We have $\max_{\underline{\Delta r}}\ \{R(\underline{\Delta r})\}\sim\min_{\underline{\Delta r}}\ \{S_2(\underline{\Delta r})\}$ and we only need to minimize $S_2(\underline{\Delta r})$ for a fixed Δt. From Eqs. (3)–(9), we find that the minimization condition is: $\nabla S_2(\underline{\Delta r})=0$ so that $\frac{\Delta x_{\max}}{\Delta t}=\mu_x$; $\frac{\Delta y_{\max}}{\Delta t}=\mu_y$. We thus see that the cross correlation techniques used to estimate AMV's do indeed correspond to the mean advection in the region considered. In contrast, if the spectra are used to estimate the advection from (k_x, ω) and (k_y, ω) sections, using Eq. (20), we estimate the μ'' velocities which are related to the μ velocities measured by AMV's by an extra normalization factor (however these represent an average over the total sample, as we will see in the next section).

5. Intermittency

5.1. Cascades

Up until now, we have used Fourier techniques since these are straightforward, well understood and allowed us to

Please cite this article as: Pinel, J., et al., The horizontal space–time scaling and cascade structure of the atmosphere and satellite radiances, Atmos. Res. (2014), http://dx.doi.org/10.1016/j.atmosres.2013.11.022

validate the basic space–time turbulence model. The main limitation is that spectra are second order statistics so that – unless the statistics are quasi-Gaussian – they only give a partial description of the process. In order to obtain a full description, we must consider statistics of all orders; this takes into account intermittency. A full validation necessitates a characterization of the flux φ which, in this model is the result of a multiplicative cascade process. In such processes, a large (“mother”) eddy breaks up into smaller (“daughter”) eddies, transferring to each of them a fraction of its turbulent flux φ, according to a stochastic rule. The process is scale invariant and repeats down to smaller and smaller scales (until scales at which viscosity becomes dominant are reached). The resulting flux at resolution Δx, scale ratio λ will have the following statistics in which different moments and intensities generally have different scaling behaviors (Schertzer and Lovejoy, 1987):

$$M_q=\frac{\langle\varphi_\lambda^q\rangle}{\langle\varphi_1\rangle^q}=\lambda'^{K(q)};\quad \lambda'=\frac{L_{\mathrm{eff}}}{\Delta x}=\frac{\lambda}{\lambda_{\mathrm{eff}}};\quad \lambda=L_{\mathrm{w}}/\Delta x;\quad \lambda_{\mathrm{eff}}=L_{\mathrm{w}}/L_{\mathrm{eff}}\tag{24}$$

where $K(q)$ is the multi-scaling exponent, L_{eff} is the effective outer scale of the cascade, $L_w\approx L_e=20000$ km is the size of the earth and λ is the scale ratio with respect to the reference scale and λ' with respect to the effective outer (largest) cascade scale in which is determined empirically. $<\varphi_1>$ is the large scale mean of the flux and serves as a normalization, nondimensionalization factor. “<.>” means ensemble average. For temporal analysis, instead of using L_w, we can use a reference time scale $\tau_{ref}=$ the duration of our sample. Eq. (24) states that for a pure cascade, plotting the log of the normalized statistical moments versus the log of the scale ratio should yield straight lines with slopes $K(q)$ and these lines should intersect at L_{eff} (or in the time domain, τ_{eff}). These stochastic multiplicative cascades are the generic multifractal process and $K(q)$ is a convex function. For the “generator” of the cascade (i.e. the logarithm of the multiplicative factors determining how φ is transferred from one scale to another at each step of the cascade), we can apply the additive central limit theorem (Schertzer and Lovejoy, 1987, 1997), so that K(q) can be expressed as a stable and attractive (universal) form depending on two parameters:

$$K(q)=\frac{C_1}{\alpha-1}\left(q^\alpha-q\right)\tag{25}$$

where C_1 is the “codimension” of the mean (i.e. a measure of the sparseness of the dominant contribution to the mean flux) and α $(0\le\alpha\le2)$ is the (Lévy) index of multifractality. For $\alpha<2$, this is only valid for $q>0$; for $q<0$, the moments diverge.

5.2. The space–time cascade structure of MTSAT and TRMM radiances

5.2.1. MTSAT radiance cascade structure

To quantify the intermittency of the cascade, we calculate the statistical moments of φ as a function of spatial (or temporal) scale Δx and see if they follow Eq. (24). Since MTSAT was over-sampled in the east–west direction (Kigawa and Sullivan, 1998), there was spurious lower variability at the smallest scale (5 km) and we therefore spatially averaged the data to 10 km resolution. We then estimated the normalized flux (see eq.1):

$$\varphi'=\frac{\varphi}{\langle\varphi\rangle}=\frac{\Delta I}{\langle\Delta I\rangle}.\tag{26}$$

The fluctuation in the field was estimated as $\Delta I=Max\{|I(x+l,y)-I(x,y)|,|I(x,y+l)-I(x,y)|\}$ for each pixel where x and y are coordinates in east–west and north–south directions respectively and $l=10$ km, the resolution at which the flux was estimated (I is the thermal IR radiance intensity measured by MTSAT). The “max” was used to partially compensate for residual measurement artifacts (excessive small scale smoothness). This improved the scaling somewhat at the smallest scales, but is not essential.

We can verify the predictions of the cascade model (Eq. (24)) by simply degrading (i.e. by spatial or temporal averaging) the resolution of the flux, taking ensemble averages of different powers of the flux for each scale of the degradation process (we took 10 points per order of magnitude of scales, equally spaced on a log scale). Fig. 6 shows the results for the zonal and meridional directions. The “effective” outer spatial scales of the cascade are found to be $L_{\mathrm{eff}}=50000$ km and 32000 km in the east–west and north–south directions respectively, i.e. somewhat larger than planetary scales. This is possible because even at planetary scales there are nonlinear interactions with other atmospheric fields, which are responsible for the additional planetary scale variability. We see that for spatial analyses, the predictions of the cascade model are well verified for smaller scales, up to ~6000 and 2000 km for east–west and north–south directions respectively; for scales beyond this we observe deviations from pure scaling. The upper scaling regime limit is smaller than L_{eff} (the outer cascade limit) and is comparable to the outer spectral scales L_d (5000 km and 2500 km for E–W and N–S directions respectively) from the spectral method in Section 3 (Table 1). These large scale deviations may be at least partly due to the anisotropy discussed earlier. Therefore, it is interesting to average the moments in both directions: $M_q^{(EWNS)}=\frac{M_q^{(EW)}+M_q^{(NS)}}{2}$. When this is done (Fig. 4), we observe almost perfect scaling over the available range of scales. Note that all of the following M~~subscript~~ q plots, the q > 1 curves lie above the axis and the q < 1 below it.

For the temporal analysis, we had to deal with an extra complication due to the resolution of the data. MTSAT images are taken every hour, but the radiances are not *averaged* over 1 h (i.e. they are basically snapshots). However, it is the resolution in *space–time* that is important: averaging snapshots in space at resolution L has the same space–time resolution as averaging data with very small spatial resolution in time over durations $\tau=L/V_w$ where V_w is the velocity estimated from the spectrum i.e. ≈40 km/h. In order to sample at the appropriate time scale and to keep the highest resolution possible, we averaged our estimated flux over a 30 km scale.

In Fig. 4, we observe that up to about ~2 days, the data are well described by the model, beyond which we observe significant deviations from scaling (the effective outer cascade scale τ_{eff} ~48 days estimated by regression is the outer scale

Please cite this article as: Pinel, J., et al., The horizontal space–time scaling and cascade structure of the atmosphere and satellite radiances, Atmos. Res. (2014), http://dx.doi.org/10.1016/j.atmosres.2013.11.022

required so that the smaller scale statistics are accurate). As mentioned earlier, atmospheric dynamics undergoes a drastic change in its variability from a *weather* regime at time scales less than ~10 days to a *macroweather* regime at larger scales (the latter going up to scales ~10–30 years, (Lovejoy and Schertzer, 2013; Lovejoy, 2013, Lovejoy et al 2013). As expected, the MTSAT data exhibit a breakdown in the scaling, but at scales a little bit smaller than this (2 days), even though it is not completely obvious to determine the transition scale from these curves. Here we see a large spread between the outer cascade scale (48 days) and the scale where the cascade scaling becomes poor (~2 days) and the scale at which the spectral scaling breaks down (~4 days, see Table 1). At small time scales – the weather regime – the statistics of the turbulent flux are described by a cascade. At larger scales – the macroweather – the spatial degrees of freedom are effectively quenched and there is a “dimensional transition” leading to different, low intermittency statistics (Lovejoy and Schertzer, 2010).

5.2.2. TRMM data

In order to further substantiate this space–time scaling model, we also used Tropical Rain Measuring Mission (TRMM) data. The TRMM satellite was launched in 1997 by the National Aeronautics and Space Administration (NASA) to monitor the atmosphere in tropical regions. Its orbit is between ±38° of latitude at an altitude of 350 km, (period ~90 min; average return period ~2 days. See Fig. 5). The satellite measures radiances in 5 bands in infrared and visible (VIRS) – at wavelengths: 12.2 μm; 10.8 μm; 3.75 μm; 1.60 μm and 0.63 μm – as well as in the microwave region (TMI) at frequencies 10.65 GHz, 19.35 GHz, 21.3 GHz, 37 GHz and 85.5 GHz. TRMM thus has the advantage (over MTSAT) of providing access to larger scales (in the zonal direction) as well as extra wavelengths not provided by MTSAT. The VIRS instrument is primarily sensitive to clouds whereas TMI is a radiometer that is also sensitive to rain (NASDA, 2001). Below, we analyzed 359 days in 1998 of VIRS channel 5 (~12.2 μm, sensitive to the temperature near the top of clouds, resolution 2.2 km, swath width 720 km) and TMI channel 8 (85.5 GHz, that has a strong signal from rain, resolution 4.4 km, swath width 760 km).

When analyzing TRMM radiances, we degraded the data resolution by a factor 2 before estimating the fluxes (in order to avoid possible spuriously smooth data at highest resolution). In order to investigate the temporal scaling in the weather and low-frequency weather regimes, we averaged the data at resolutions 1 day and 100 km in time and space (see Fig. 5). The return period of the satellite is shorter at higher latitudes

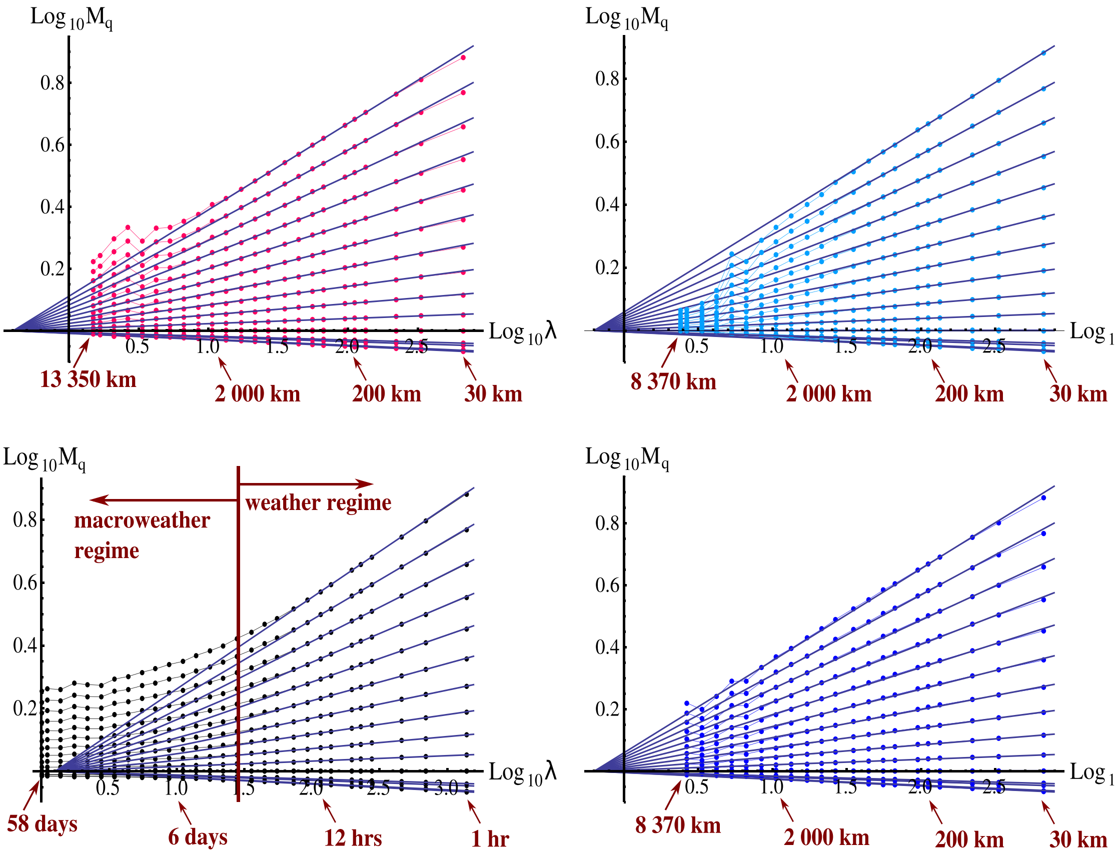

Fig. 4. Log–log plot of the moments M_q of the normalized flux φ' for MTSAT thermal IR as a function of the scale ratio λ (dots correspond to data). Each curve corresponds to a single value of q, from $q = 0$ at the bottom to $q = 3$ at the top, by steps of 0.2 ($q > 1$ curves are above the axis, $q < 1$ are below). Straight blue lines are a fit with the constraint that they all intersect at a unique scale, L_{eff}. Each graph corresponds to a different direction in which the degradation of the resolution was done. Top-left: east–west, $L_{\mathrm{eff}} = 50000$ km. Top-right: north–south, $L_{\mathrm{eff}} = 32000$ km. Bottom-left: time, $\tau_{\mathrm{eff}} = 48$ days. Bottom-right: average of east–west and north–south directions, $L_{\mathrm{eff}} = 32000$ km. (For interpretation of the references to color in this figure legend, the reader is referred to the web version of this article.)

Please cite this article as: Pinel, J., et al., The horizontal space–time scaling and cascade structure of the atmosphere and satellite radiances, Atmos. Res. (2014), http://dx.doi.org/10.1016/j.atmosres.2013.11.022

from the equator and can be as much as 4 days for certain areas near the equator. The space–time resolutions were thus chosen as a compromise, so the analysis could benefit from the highest temporal resolution possible while having enough values to provide a good spatial average on and reasonable statistics. We rejected every resulting 100 km pixel having less than a critical fraction (75%) of data coverage. Similarly, when testing Eq. (24) for different spatial or temporal resolutions, we rejected degraded pixels with more than 25% missing values.

5.2.3. TRMM radiance cascade structure

Figs. 6 and 7 show the results for VIRS-5 and TMI-8. For VIRS-5, we see that for the east–west spatial analysis, predictions of our cascade model are generally well verified except for small deviations at small scales for high order statistical moments. The outer scale is $L_{\mathrm{eff}} = 25\,000$ km, a little smaller than for MTSAT (~50000 km) in the same direction. The scaling in the north–south direction is not as good with additional, although small, deviations at larger scales. The outer scale of the north–south cascade is $L_{\mathrm{eff}} = 12\,600$ km, again smaller than what we found for MTSAT. For the temporal analysis, we observe that Eq. (24) gives an accurate description (with an outer scale $\tau_{\mathrm{eff}} = 57$ days) for small scales, up to ~14 days, scale beyond which, once again, we observe significant deviations from scaling, (corresponding to a transition towards a different scaling regime see Table 1.)

For TMI-8, the cascade model predictions are well followed for spatial scales up to 4000 and 2000 km for east–west and north–south directions respectively. At larger scales, we observe slight deviations from pure scaling. Similarly to MTSAT and VIRS-5, the north–south moments have lower variability than predicted by the cascade model at large scales, while the variability of east–west moments is slightly higher than the model predictions. The outer scales are $L_{\mathrm{eff}} = 12\,600$ km and 8000 km for east–west and north–south directions respectively; scales smaller than for MTSAT and VIRS-5. For the temporal direction, we can identify a weather regime at small scales (<4 days), even though there are only a few data points. The outer scale is $\tau_{\mathrm{eff}} = 57$ days, just like VIRS-5. For time scales larger than 4 days, we observe the usual transition.

We can compare these values with analyses of VIRS-5 and TMI-8 data in the satellite orbit direction made by Lovejoy et al. (2009d) at higher resolutions (8.8 km and 13.9 km for VIRS-5 and TMI-8 respectively) from the months of January and February 1998 (Table 1). Interestingly, the values of L_{eff} and L_d found in their analyses are comparable with our values in the north–south direction.

5.2.4. Estimating C_1 and α

From Figs. 4, 6 and 7 we can estimate the multi-scaling exponent $K(q)$ with the parameter C_1 and α for the three directions (east–west, north–south, time). We see from Fig. 8 that the intermittency of MTSAT data is nearly the same in all directions. Similarly to MTSAT, the intermittency of the VIRS-5 and TMI-8 fluxes is almost isotropic (Fig. 8), with small differences in the different directions for higher statistical order. We estimate C_1 using $C_1 = K'(1)$ (see Eq. (25)). All the values are close to each other and are comparable to those found by Lovejoy et al. (2009d) (although our value for TMI-8 is a little bit smaller, see Table 1.)

With the help of Eq. (25), we can also estimate the parameter α by calculating the "reduced moments": $M_q' = M_q^{(\alpha-1)/(q^\alpha - q)} = \lambda^{C_1}$. If the log of the moments follows Eqs. (24) and (25), all the curves should collapse – the "Lévy collapse" – onto a single curve λ^{C_1} (up to a critical value q_c beyond which $K(q)$ becomes linear, expressing the fact that either the moments of order $q > q_c$ are dominated by the maximum value in a finite sample). We can estimate α for the cascade by identifying the value for which we find the best collapse. The values of α for our three datasets vary, though they are all ≥ 1.5. (see Fig. 9 and Table 1).

5.3. Probability distributions of MTSAT and TRMM radiance fluxes

In the last section, in order to study the intermittency, we presented a detailed analysis of the statistical moments of radiance fluxes. We can also, in an equivalent way, describe the fluxes by looking at their probability distributions. A general prediction of cascade models is that their extreme

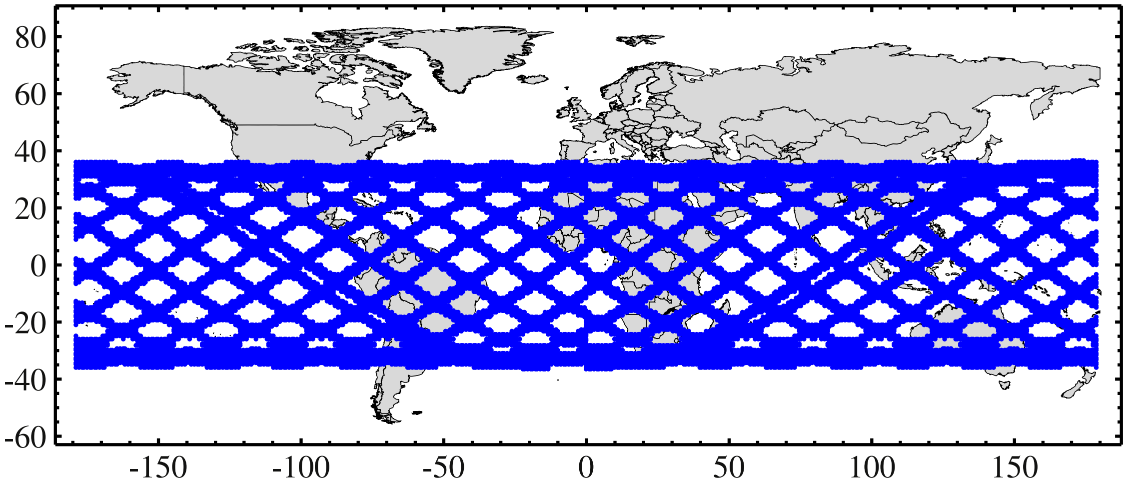

Fig. 5. One day (i.e. ~16 orbits, in blue) of TRMM VIRS-5, (2.2 km resolution) degraded at 100 km resolution. The temporal resolution is higher near ±38°.

Please cite this article as: Pinel, J., et al., The horizontal space–time scaling and cascade structure of the atmosphere and satellite radiances, Atmos. Res. (2014), http://dx.doi.org/10.1016/j.atmosres.2013.11.022

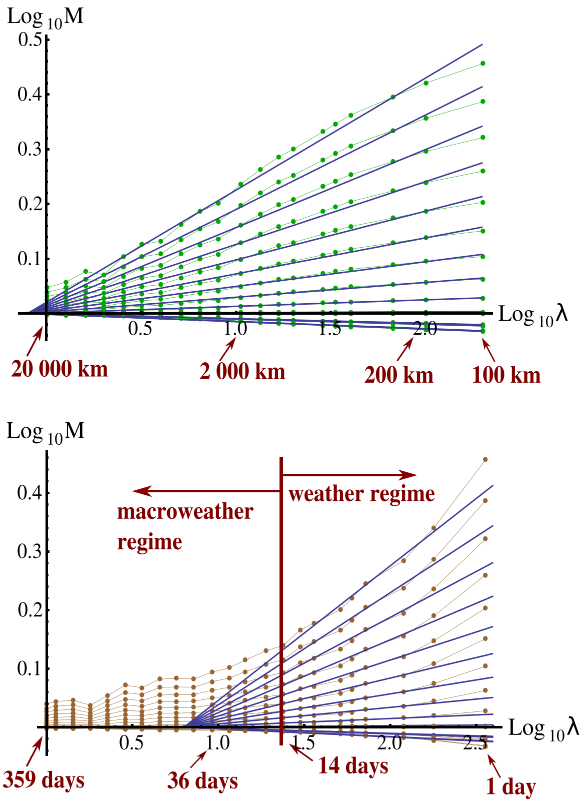

Fig. 6. Log–log plot of the moments M_q of the normalized flux φ' for VIRS-5 as a function of the scale ratio λ (dots correspond to data). Each curve corresponds to a single value of q, from $q = 0$ at the bottom to $q = 2.8$ at the top, by step of 0.2. Straight blue lines are a fit with the constraint that they all intersect at a unique scale, L_{eff}. Each graph corresponds to a different direction in which the degradation of the resolution was done. Top-left: east–west, $L_{\mathrm{eff}} = 25000$ km. Top-right: north–south, $L_{\mathrm{eff}} = 12600$ km. Bottom-left: time, $\tau_{\mathrm{eff}} = 57$ days. (For interpretation of the references to color in this figure legend, the reader is referred to the web version of this article.)

probability tails are “hyperbolic” or “fat-tailed” (Mandelbrot, 1974):

$$\Pr(\varphi > s) \sim s^{-q_D} \quad ; \quad s \gg 1 \quad ; \quad q > q_D. \tag{27}$$

The value q_D depends on the cascade, but also on the space–time dimension D over which the cascade is averaged. Distributions with an exponent q_D have statistical moments that diverge for all orders $q > q_D$. If the sample size is sufficiently large, we can observe this hyperbolic tail as a straight line on a log–log plot. Fig. 10 shows the results for MTSAT and TRMM fluxes. While VIRS-5 and TMI-8 fluxes fairly convincingly exhibit this hyperbolic behavior with $q_D \approx 7$, MTSAT fluxes have distributions which fall off much more rapidly. In comparison, Lovejoy and Schertzer (2013) present a summary of similar analyses including horizontal wind for which $q_D = 5$–7.5 and temperature for which $q_D = 4.5$–5.5 was found. The existence of hyperbolic tails has theoretical implications since it means that certain cascade models such as Log–Poisson (Schertzer et al., 1995) or microcanonical (Lovejoy, 2010) cascades can be ruled out.

5.4. Space–time statistical relations from atmospheric radiance fluxes

In order to further characterize the space–time statistics, we may estimate the Eulerian size/lifetime statistical relations. A One method is to find a correspondence between spatial and temporal resolution for which the variability is the same:

$$\left\langle \varphi^q_{\tau_{ref}/\tau} \right\rangle = \left\langle \varphi^q_{L_{ref}/L} \right\rangle \tag{28}$$

i.e. implicit relations between τ and L. The fact that the $K(q)$ functions are close for space and time shows that this relation is independent of q and that there is a constant value – with the dimensions of a velocity – describing this space–time relation. If the scaling were perfect with identical $K(q)$ in space and time, we would obtain:

$$V_{eff} = \frac{L_{\mathrm{eff}}}{\tau_{\mathrm{eff}}}. \tag{29}$$

To test this, we may estimate V_{eff} by superposing the curves from Figs. 4, 6 and 7 and horizontally shift one set of

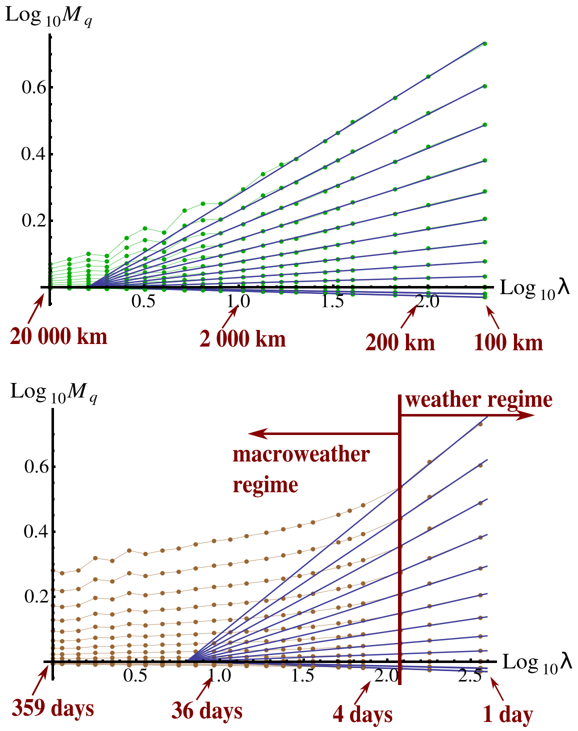

Fig. 7. Log-log plot of the moments M_q of the normalized flux φ' for TMI-8 as a function of the scale ratio λ (dots correspond to data). Each curve corresponds to a single value of q, from $q = 0$ at the bottom to $q = 2.8$ at the top, by step of 0.2. Straight blue lines are a fit with the constraint that they all intersect at a unique scale, L_{eff}. Each graph corresponds to a different direction in which the degradation of the resolution was done. Top-left: east–west, $L_{\text{eff}} = 12600$ km. Top-right: north–south, $L_{\text{eff}} = 8000$ km. Bottom-left: time, $\tau_{\text{eff}} = 57$ days. (For interpretation of the references to color in this figure legend, the reader is referred to the web version of this article.)

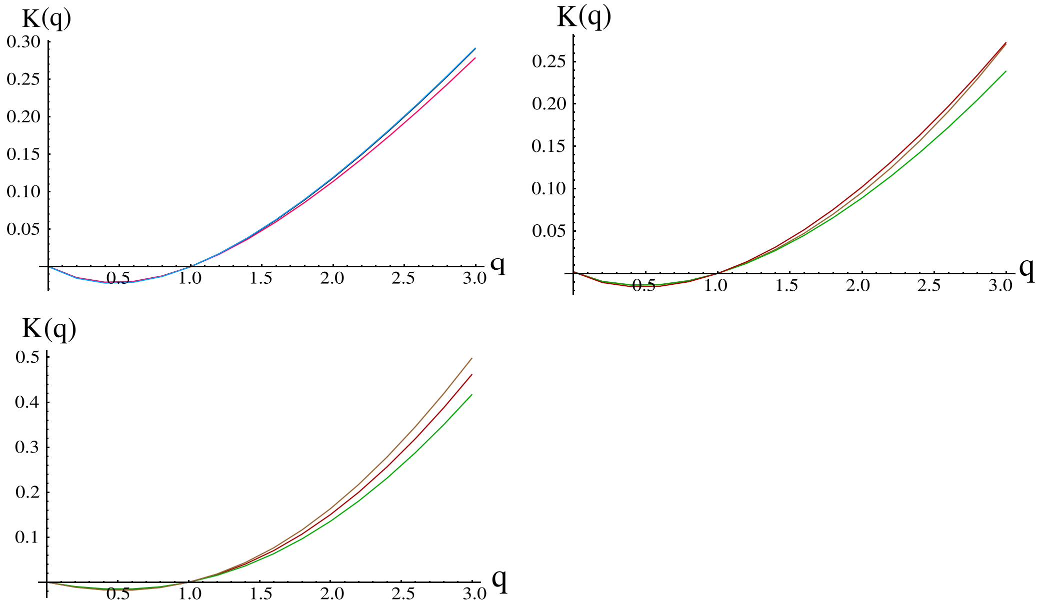

Fig. 8. Top-left: characterization of the intermittency of MTSAT thermal IR turbulent flux by its moment scaling exponent $K(q)$ estimated from Fig. 4. In blue: north–south direction, $C_1 = 0.07$. In magenta: east–west direction, $C_1 = 0.07$. In black (superposed to the north–south curve exactly): in time, $C_1 = 0.07$. Top-right: characterization of the intermittency of VIRS-5's turbulent fluxes by its moments scaling exponent function $K(q)$ estimated from Fig. 6. In red: north–south direction, $C_1 = 0.06$. In green: east–west direction, $C_1 = 0.05$. In brown: temporal direction, $C_1 = 0.05$. Bottom: Characterization of the intermittency of TMI-8's turbulent fluxes by its moments scaling exponent function $K(q)$ estimated from Fig. 7. In red: north–south direction, $C_1 = 0.06$. In green: east–west direction, $C_1 = 0.05$. In brown: temporal direction, $C_1 = 0.08$. (For interpretation of the references to color in this figure legend, the reader is referred to the web version of this article.)

Please cite this article as: Pinel, J., et al., The horizontal space–time scaling and cascade structure of the atmosphere and satellite radiances, Atmos. Res. (2014), http://dx.doi.org/10.1016/j.atmosres.2013.11.022

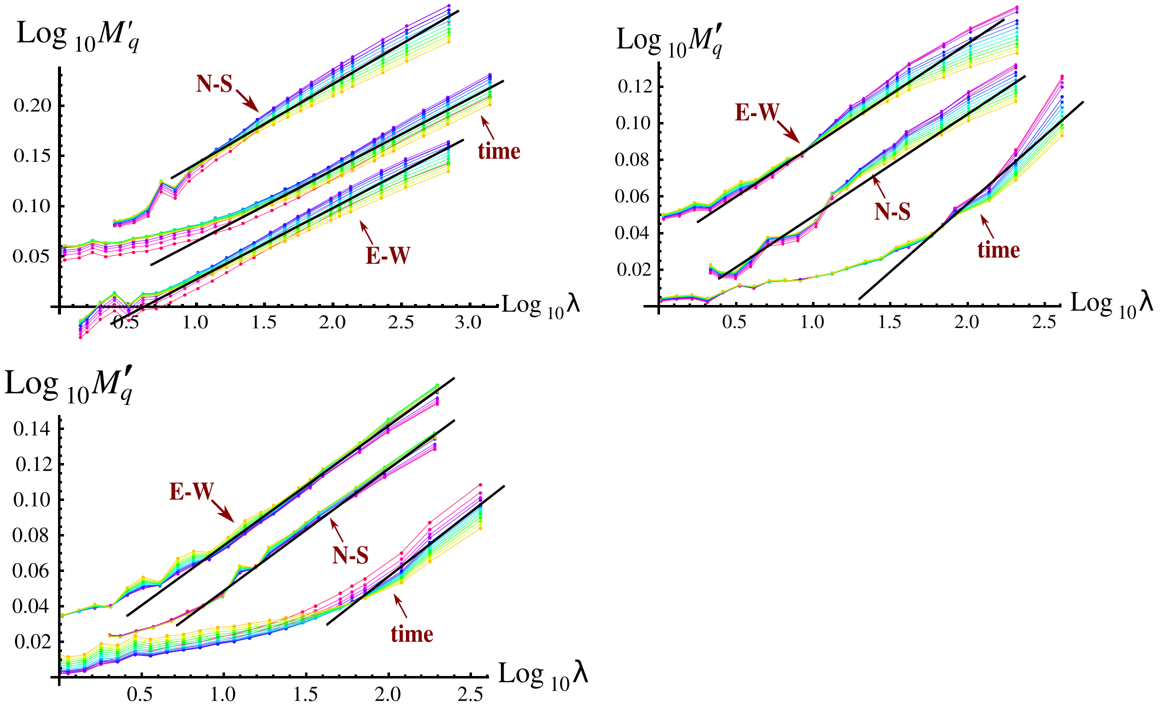

Fig. 9. Levy collapse using the value of α that minimizes the deviations. Top-left: MTSAT IR fluxes: α ~ 1.5–1.6. Top-right: VIRS-5 fluxes: α ~ 1.8. Bottom: TMI-8 fluxes: α ~ 2.2 (since theoretically $\alpha \leq 2$, presumably, α ~ 2). Note that the reference scale (corresponding to $\lambda = 1$) in the spatial analyses was 20000 km whereas in time it was 2 months (MTSAT) and 359 days (VIRS-5, TMI-8).

curves (spatial or temporal), such as to make them overlap as much as possible (Figs. 11, 12 and 13). From this shift, we can identify the relation between L and τ (giving the same variability) and can extract V_{eff}. We found for MTSAT (Fig. 10) $V_{eff} = 33$ km/h $= 792$ km/day (average of east–west and north–south directions), comparable with V found from spectral methods (~40 km/h ≈ 1000 km/day, see Table 1). This effective velocity implies that a structure in the flux of size 33 km will “live” for 1 h. These velocities are typical values of turbulent wind in the atmosphere (~36 km/h = 10 m/s). Although a linear relation between spatial and temporal statistics follows if the turbulence is “frozen”; our interpretation is quite different. In “frozen turbulence”, relative motion within structures is negligible and V_{eff} is a constant deterministic advection velocity whereas in our case, V_{eff} is a turbulent velocity (e.g. an RMS velocity). Similarly, we can compare statistics in east–west and north–south directions, a relation expressed with the parameter a that describes the horizontal

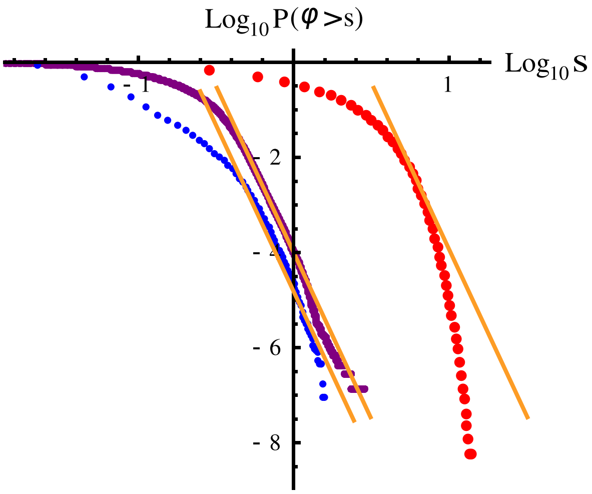

Fig. 10. Probability distributions for the radiances fluxes exceeding a fixed threshold s. In red: MTSAT fluxes at 30 km, 1 h resolutions. In purple: VIRS-5 fluxes at 100 km, 1 day resolutions. In blue: TMI-8 fluxes at 100 km, 1 day resolutions. The orange reference lines all have absolute slopes $q_D = 7$. (For interpretation of the references to color in this figure legend, the reader is referred to the web version of this article.)

Please cite this article as: Pinel, J., et al., The horizontal space–time scaling and cascade structure of the atmosphere and satellite radiances, Atmos. Res. (2014), http://dx.doi.org/10.1016/j.atmosres.2013.11.022

space trivial (scale independent) anisotropy. We found that $a \approx 1.2$ so that structures are typically 1.2 times wider (E–W) than their N–S extents (c.f. the value $a \sim 1.2$ from MTSAT IR spectra; see Table 1).

Figs. 12 and 13 show the corresponding matches of statistical moments for VIRS-5 and TMI-8. From the shift applied, we can extract an effective velocity: $V_{eff} = 14$ km/h = 336 km/day and for $V_{eff} = 5$ km/h = 120 km/day for VIRS-5 and TMI-8 respectively, smaller than for MTSAT (Table 1). The spatial anisotropy parameters a are on the contrary all comparable.

We can also compute the Eulerian space–time diagrams and their spatial counterparts, space–space diagrams (see Fig. 14) for MTSAT and VIRS-5 fluxes. Unfortunately, as can be seen in Fig. 13, in the case of TMI-8 we only have three data points in the weather regime which is insufficient for a reliable estimate. From Figs. 4 and 6, we chose an order of statistical moment ($q = 1.8$) that is well estimated and, from the values of the chosen moment, we found a correspondence between spatial and temporal lags (for which the moments are the same). We see in Fig. 14 straight lines with slopes 1, reflecting the good scaling we obtained in Figs. 4 and 6. A structure ≈100 km zonal extent will therefore on average last 3 h, a ≈ 1000 km structure (a little bit less in the meridional direction) will last 30 h, etc. From Fig. 14, we can also estimate the parameters V_{eff} and a. We found values all consistent with those found from the previous method, when shifting all the moments (for MTSAT: $V_{eff} \sim 33$ km/h = 792 km/day and $a = 1.5$—for VIRS-5: $V_{eff} = 14$ km/h = 336 km/day and $a = 1.5$).

6. Conclusions

Understanding the space–time statistical behavior of atmospheric fields as functions of scale is a fundamental yet unsolved problem. Indeed, it is troubling that in spite of the plethora of data now available, there is no agreement about the theoretical or empirical space–time statistical properties of the atmosphere including their power spectra. However, we argue that over wide ranges, the atmospheric spatial variability is well described by an anisotropic scaling model where two different scaling laws apply in the horizontal and vertical. In this model, no scale separation exists and Taylor's frozen turbulence hypothesis is not justified. Since in the Eulerian frame advection is the key ingredient in relating spatial to temporal statistics, this anisotropic spatial scaling will have direct consequences for the temporal scaling.

We discussed this theoretically, making the assumption that the largest (planetary scale) eddies advect the smaller ones, averaging over these random advections. The result is that the structure functions and spectra are both power laws of scale functions, themselves approximately quadratic forms in (x, y, t) and (k_x, k_y, ω) spaces respectively. The parameters depended on the mean advection velocity as well as the turbulent velocity and a mean north–south/east–west aspect ratio.

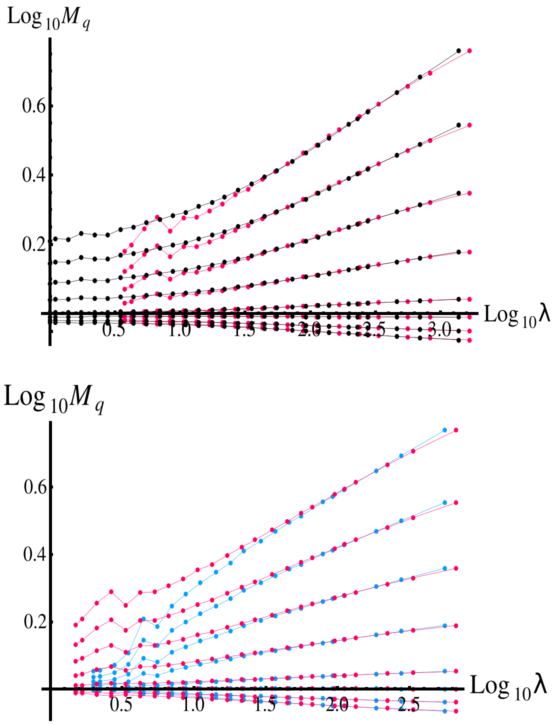

Fig. 11. Comparison of statistical moments of radiances fluxes. One set of curves is shifted to match the other set. An effective velocity V_{eff} is extracted from that shift, characterizing the statistical size/lifetime relation for atmospheric structures measured by MTSAT. Upper-left: space (east–west: magenta) vs time (black), $V_{eff} = 36$ km/h. Upper-right: space (north–south: blue) vs time (black), $V_{eff} = 30$ km/h. Bottom: space (north–south: blue) vs space (magenta), $a = 1.2$ (characterizing horizontal trivial anisotropy). Values of q shown: 0.0; 0.4; 0.8; 1.2; 1.6; 2.0; 2.4; 2.8. (For interpretation of the references to color in this figure legend, the reader is referred to the web version of this article.)

Please cite this article as: Pinel, J., et al., The horizontal space–time scaling and cascade structure of the atmosphere and satellite radiances, Atmos. Res. (2014), http://dx.doi.org/10.1016/j.atmosres.2013.11.022

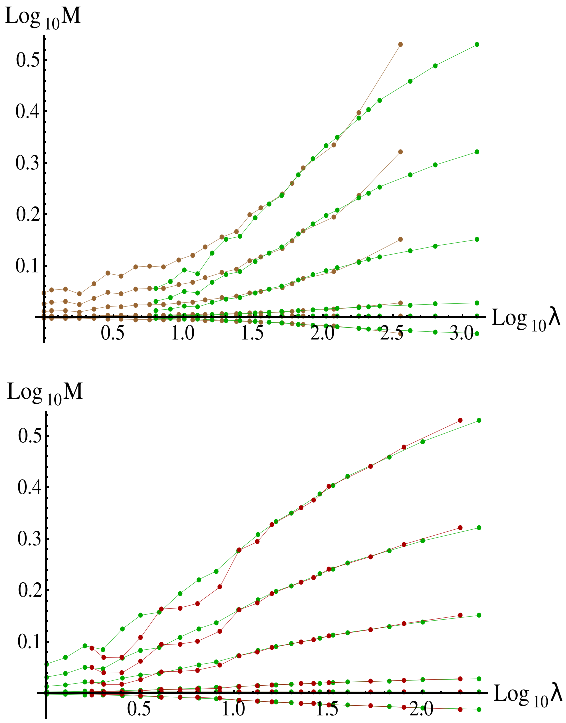

Fig. 12. Comparison of statistical moments of VIRS-5's fluxes. One set of curves is shifted to match the other set. An effective velocity V_{eff} is extracted from that shift, characterizing the statistical size/lifetime relation for atmospheric structures measured by VIRS-5. Upper left: space (east–west: green) vs time (brown), $V_{eff} = 15$ km/h. Upper right: space (north–south: red) vs time (brown), $V_{eff} = 12$ km/h. Bottom: space (north–south: red) vs space (green), $a = 1.3$ (characterizing horizontal trivial anisotropy). Values of q shown: 0.0; 0.6; 1.0; 1.6; 2.2; 2.8. (For interpretation of the references to color in this figure legend, the reader is referred to the web version of this article.)

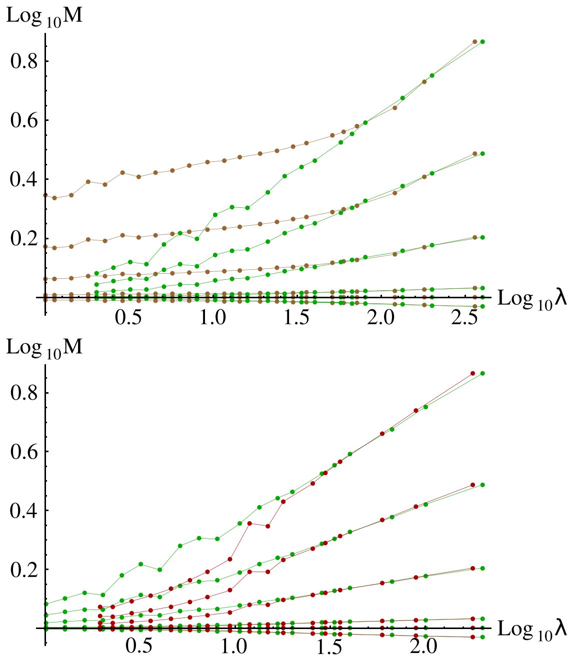

Fig. 13. Comparison of statistical moments of TMI-8's fluxes. One set of curves is shifted to match the other set. An effective velocity V_{eff} is extracted from that shift, characterizing the statistical size/lifetime relation for atmospheric structures measured by TMI-8. Upper left: space (east–west: green) vs time (brown), $V_{eff} = 5$ km/h. Upper right: space (north–south: red) vs time (brown), $V_{eff} = 5$ km/h. Bottom: space (north–south: red) vs space (green), $a = 1.1$ (characterizing horizontal trivial anisotropy). Values of q shown: $q = 0.0$; 0.6; 1.0; 1.6; 2.2; 2.8. (For interpretation of the references to color in this figure legend, the reader is referred to the web version of this article.)

Please cite this article as: Pinel, J., et al., The horizontal space–time scaling and cascade structure of the atmosphere and satellite radiances, Atmos. Res. (2014), http://dx.doi.org/10.1016/j.atmosres.2013.11.022

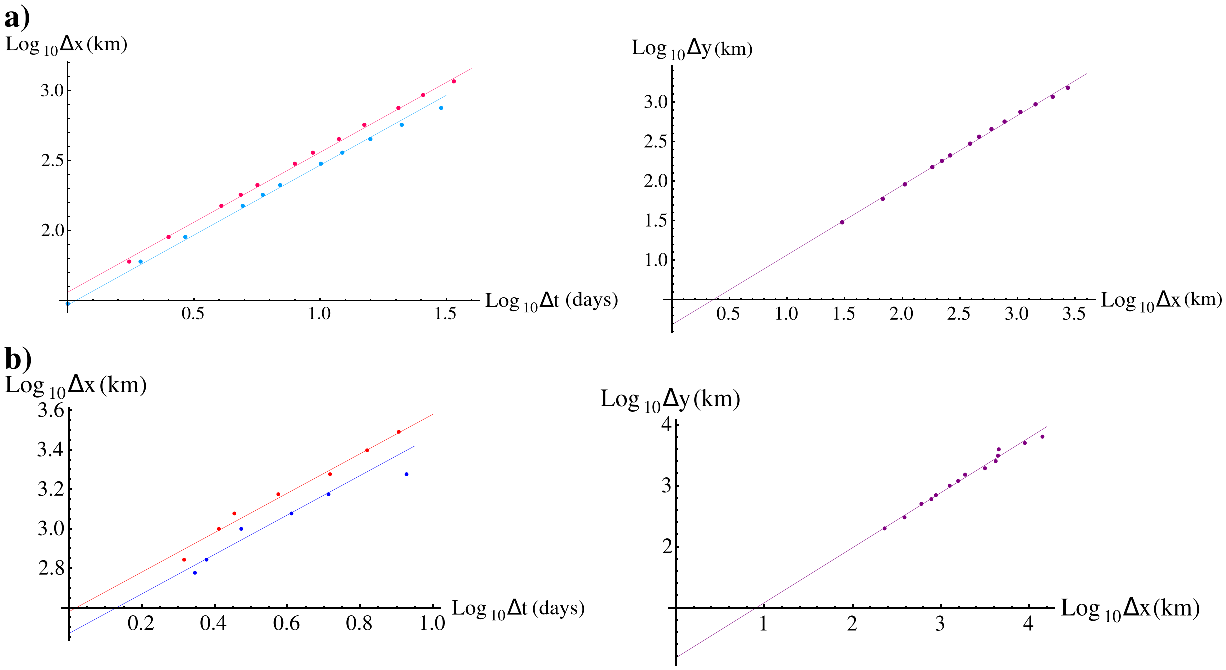

Fig. 14. a) Left: space–time diagram for $q = 1.8$ and $\Delta t < 63$ h (belonging to the weather regime) for MTSAT fluxes. Magenta: east–west direction; $V_{eff} = 36$ km/h. Blue: north–south direction; $V_{eff} = 30$ km/h. Right: MTSAT fluxes space-space diagramme for $q = 1.8$; $a = 1.5$. b) Left: space–time diagramme for $q = 1.8$ and $\Delta t < 8$ days (~weather regime) for VIRS-5 fluxes. Magenta: east–west direction; $V_{eff} = 16$ km/h. Blue: north–south direction; $V_{eff} = 12$ km/h. Right: VIRS-5 fluxes space–space diagramme for $q = 1.8$; $a = 1.5$. Reference lines have slope = 1 corresponding to linear space–time and space–space relations. (For interpretation of the references to color in this figure legend, the reader is referred to the web version of this article.)

The theory was tested on 1-D and 2-D spectral cross-sections using infrared radiances measured by geostationary satellites which allow us to estimate space–time statistics over wide ranges of scale. Estimating spectra from infrared MTSAT data, we found that our theoretical spectra accurately reproduce the observed 3D (k_x, k_y, ω) spectral density over the range 2 h to ≈100 h and 60 km to ≈5000 km. Multivariate regressions provided the best fit parameters $\tau_w \sim 20 \pm 1$ days (using $L_w \sim L_e = 20000$ km), the mean lifetime of planetary structures, $V_w \sim 41 \pm 3$ km/h, their typical relative velocity as well as the average overall advections in zonal ($\overline{v_x} \sim -12 \pm 4$ km/h ≈ −300 km/day) and meridional ($\overline{v_y} \sim 4 \pm 3$ km/h ≈ 100 km/day) directions over a ~2 month period for a region centered slightly south of the equator in the western Pacific. The 1D spectral exponents were the same in the three space-time directions (implying horizontal space–time isotropy for the exponents), with $\beta \sim 1.55 \pm 0.01$, comparable to the passive scalar, Corrsin–Obukhov value with intermittent corrections ($\beta = 5/3 - K(2) \approx 1.55$). While the data comes primarily from the tropics, we consider high level emergent statistical laws; there is no reason to assume that they contradict the usual (lower level, deterministic) laws of tropical meteorology.

Spectra are only second order statistics; to obtain a more complete description, we found that we can describe atmospheric radiances (including TRMM's infrared and passive microwave) turbulent flux statistics by a multiplicative cascade model over large ranges of spatial scales with typically slight deviations at small and large scales. Analogous temporal analyses showed similar agreement at small scales, but with significant deviations at scales larger than a few days (2 to 14 days), marking two regimes. It was proposed that these two regimes are separated by this temporal scale break (associated with planetary scales in space) and could be identified as a "weather regime" at short time scales and a "macroweather" regime at longer time scales, providing a concrete way to characterize the dynamical processes associated with weather and determine their corresponding space–time scales. (This break in the scaling symmetry is also present in the temporal spectrum, although only for the few low frequency data points.) With the help of a multiplicative cascade model, we were able to describe how the space–time statistics change with scale with the help of only a few parameters C_1 (the intermittency near the mean), α (the degree of multifractality), L_{eff} (the effective outer spatial scale), V_{eff} (the effective space–time transformation speed) and a (the zonal/meridional aspect ratio). Although the values of C_1 and a are all close to each other for our three data sets (MTSAT, VIRS-5 and TMI-8), we observe some differences in the remaining parameters. The values of L_{eff} are somewhat different for the three datasets, but its values (in the north–south direction) are comparable to those obtained by Lovejoy et al. (2009d) (along with C_1) in the direction of the orbit of the satellite. The three datasets were associated with different wavelengths and were sensitive to different types of structures (rain, clouds, etc.). The parameter α which gives a measure of how "extreme" (or multifractal) is the field was found to vary between 1.5 and 2. We also showed that TRMM's VIRS-5 and TMI-8 fluxes exhibit nonclassical behavior regarding the extreme values in the fact they follow hyperbolic probability distribution with an exponent characterizing the extreme tails $q_D = 7$. MTSAT fluxes seemed to involve much higher values of q_D. A finite q_D rule's out some

Please cite this article as: Pinel, J., et al., The horizontal space–time scaling and cascade structure of the atmosphere and satellite radiances, Atmos. Res. (2014), http://dx.doi.org/10.1016/j.atmosres.2013.11.022

cascade models such as microcanonical and Log–Poisson cascades.

These results contribute to our understanding of atmospheric dynamics at a fundamental level, but could also be useful in applications such as improving the efficiency of meteorological measurements, as they prescribe the space–time resolutions at which these measurements should be made. This framework also provides a theoretical basis for interpreting IR satellite derived "atmospheric motion vectors" in terms of turbulent winds. Although the model presented in this paper was used to describe turbulent field statistics, it can be extended to take into account atmospheric waves as well. For this, our theoretical form can be used to determine the "turbulent background" and the residual can be interpreted in terms of waves. This follows Wheeler and Kiladis (1999) who similarly argued that atmospheric waves would be detectable from IR thermal spectral densities, after the removal of a multiplicative turbulent background. The difference is that their method of estimating the background was essentially ad hoc whereas ours is theoretically motivated. Note that in any case, whereas the background spectral density varies by 5 orders of magnitude over the scaling range, the residual varies only by a factor 2–4, so that as a first approximation (treated here), the waves can be ignored. We pursue this question in Pinel and Lovejoy, 2013, 2014.

Acknowledgements

J. Pinel acknowledges an FQRNT graduate scholarship. This work was unfunded, there are no conflicts of interest.

References

Bjerknes, J., 1969. Atmospheric teleconnections from the Equatorial Pacific. Mon. Weather Rev. 97, 163–172.

Bolgiano Jr., R., 1959. Turbulent spectra in a stably stratified atmosphere. J. Geophys. Res. 64 (12), 2226–2229. http://dx.doi.org/10.1029/JZ064i012p02226.

Chamberlain, J.W., Hunten, D.M., 1987. Theoryof Planetary Atmospheres: an Introduction to their Physics and Chemistry, Second edition. Academic Press Inc.

Charney, J.G., 1971. Geostrophic turbulence. J. Atmos. Sci. 28, 1087.

Cushman-Roisin, B., 1994. Introduction to Geophysical Fluid Dynamics. Prentice Hall.

Dias, J., Tulich, S.N., Kiladis, G.N., 2012. An object based approach to assessing tropical convection organization. J. Atmos. Sci. 69, 2488–2504.

Frehlich, R.G., Sharman, R.D., 2010. Equivalence of velocity statistics at constant pressure or constant altitude. Geophys. Res. Lett. 37, L08801 (5 PP.).

Hendon, H.H., Wheeler, M., 2008. Some space–time spectral analyses of tropical convection and planetary waves. J. Atmos. Sci. 65, 2936–2948.

Hsu, H.M., Moncrieff, M.W., Tung, W.W., Changhai, L., 2006. Multiscale temporal variability of warm-season precipitation over North-America: statistical analysis of radar measurements. J. Atmos. Sci. 63, 2355–2368.

Hsu, H.M., Lin, C.Y., Guenther, A., Tribbia, J.J., Liu, S.C., 2011. Air-chemistry "turbulence": power-law scaling and statistical regularity. Atmos. Chem. Phys. 11, 8395–8413.

Kigawa, S., Sullivan, P.C., 1998. Meteorological Satellite Center Technical Note, No.36, December.

Kolmogorov, A.N., 1941. Local structure of turbulence in an incompressible liquid for very large Reynolds numbers. English translation: Proc. Roy. Soc. A434, 9-17, 1991 Proc. Acad. Sci. URSS Geochem. Sect. 30, 299–303.

Leese, J.A., Novak, C.S., Taylor, V.R., 1970. The determination of cloud pattern motions from geosynchronous satellite image data. Pattern Recogn. 2, 279–292.

Lilley, M., Lovejoy, S., Strawbridge, K., Schertzer, D., Radkevich, A., 2008. Scaling turbulent atmospheric stratification, Part II: spatial stratification and intermittency from lidar data Quart. J. R. Meteorol. Soc. 134, 301–315.

Lindborg, E., et al., 2009. Comment on "Reinterpreting aircraft measurments in anisotropic scaling turbulence" by Lovejoy et al 2009. Atmos. Chem. Phys. Discuss. 9, 22331–22336.

Lindborg, E., et al., 2010. Interactive comment on "Comment on "Reinterpreting aircraft measurements in anisotropic scaling turbulence" by S. Lovejoy et al. (2009)". Atmos. Chem. Phys. Discuss. 9, C9797–C9798.

Lovejoy, S., 2010. Why the bare/dressed cascade distinction matters: interactive comment on "Reconstruction of sub-daily rainfall sequences using multinomial multiplicative cascades" by L. Wang et al. Hydrol. Earth Syst. Sci. Discuss. 7, C1–C4.

Lovejoy, S., 2013. What is the Climate? EOS, 94, No. 1, 1 January 2013, p1-2.

Lovejoy, S., Schertzer, D., 2010. Towards a new synthesis for atmospheric dynamics: space–time cascades. Atmos. Res. 96, 1–52 (1016/j.atmosres. 2010.01004).

Lovejoy, S., Schertzer, D., 2011. Space–time cascades and the scaling of ECMWF reanalyses: fluxes and fields. J. Geophys. Res. 116, D14117. http://dx.doi.org/10.1029/2011JD015654.

Lovejoy, S., Schertzer, D., 2012. Low frequency weather and the emergence of the Climate. In: Sharma, A.S., Bunde, A., Baker, D., Dimri, V.P. (Eds.), Extreme Events and Natural Hazards: The Complexity Perspective. AGU monograph, pp. 231–254.

Lovejoy, S., Schertzer, D., 2013. The Weather and Climate, Emergent Laws and Multifractal Cascades. Cambridge University Press, Cambridge, UK.

Lovejoy, S., Tuck, A.F., Hovde, S.J., Schertzer, D., 2007. Is isotropic turbulence relevant in the atmosphere? Geophys. Res. Lett. 34, L14802. http://dx.doi.org/10.1029/2007GL029359.

Lovejoy, S., Schertzer, D., Lilley, M., Strawbridge, K., Radkevich, A., 2008. Scaling turbulent atmospheric stratification, Part I: turbulence and waves. Q. J. R. Meteorol. Soc. 134, 277–300.

Lovejoy, S., Tuck, A.F., Schertzer, D., Hovde, S.J., 2009a. Reinterpreting aircraft measurements in anisotropic scaling turbulence. Atmos. Chem. Phys. 9, 1–19.

Lovejoy, S., Tuck, A.F., Schertzer, D., 2009b. Interactive comment on "Reinterpreting aircraft measurements in anisotropic scaling turbulence" by S. Lovejoy et al. Atmos. Chem. Phys. Discuss. 9, S2592–S2599.

Lovejoy, S., Tuck, A.F., Schertzer, D., 2009c. Interactive comment on "Comment on "Reinterpreting aircraft measurements in anisotropic scaling turbulence" by Lovejoy et al. (2009)" by E. Lindborg et al. Atmos. Chem. Phys. Discuss. 9, C7688–C7699.

Lovejoy, S., Schertzer, D., Allaire, V., Bourgeois, T., King, S., Pinel, J., Stolle, J., 2009d. Atmospheric complexity or scale by scale simplicity? Geophys. Res. Lett. 36, L01801. http://dx.doi.org/10.1029/2008GL035863.

Lovejoy, S., Tuck, A.F., Schertzer, D., 2010. The horizontal cascade structure of atmospheric fields determined from aircraft data. J. Geophys. Res. 115, D13105. http://dx.doi.org/10.1029/2009JD013353.

Lovejoy, S., Schertzer, D., Varon, D., 2013. Do GCM's predict the climate… or macroweather? Earth Syst. Dynam. 4, 1–16. http://dx.doi.org/10.5194/esd-4-1-2013.

Madden, Roland A., Julian, Paul R., 1971. Detection of a 40–50 day oscillation in the zonal wind in the tropical Pacific. J. Atmos. Sci. 28, 702–708.

Madden, Roland A., Julian, Paul R., 1972. Description of global-scale circulation cells in the tropics with a 40–50 day period. J. Atmos. Sci. 29, 1109–1123.

Madden, R.A., Julian, P.R., 1994. Observations of the 40–50 day tropical oscillation: a review. Mon. Weather Rev. 122, 814–837.

Mandelbrot, B.B., 1974. Intermittent turbulence in self-similar cascades: divergence of high moments and dimension of the carrier. J. Fluid Mech. 62, 331–350.

Marsan, D., Schertzer, D., Lovejoy, S., 1996. Causal space–time multifractal modelling of rain. J. Geophys. Res. 31D, 26, 333–26, 346.

Matsuno, T., 1966. Quasi-geostrophic motions in the equatorial area. J. Meteorol. Soc. Jpn. 44, 25–43.

NASDA, 2001. TRMM data users handbook. National Space Development Agency of Japan Earth Observation Center.

Neelin, J.D., Battisti, D.S., Hirst, A.C., Jin, F., Wakata, Y., Yamagata, T., Zebiak, S.E., 1998. ENSO theory. J. Geophys. Res. (ISSN: 0148-0227), 103. http://dx.doi.org/10.1029/97JC03424.

Obukhov, A., 1959. Effect of archimedean forces on the structure of the temperature field in a turbulent flow, Dokl. Akad. Nauk SSSR 125.

Pinel, J., 2013. The Anisotropic Space–time Scaling of the Atmosphere: Turbulence and Waves. Ph.D thesis McGill University, Montreal, Canada.

Pinel, J., Lovejoy, S., 2013. Atmospheric waves as scaling, turbulent phenomena Atmos. Chem. Phys. Discuss. 13, 14797–14822. http://dx.doi.org/10.5194/acpd-13-14797-2013.

Pinel, J., Lovejoy, S., 2014. Atmospheric waves as scaling, turbulent phenomena. Atmos. Chem. Phys. (accepted for publication).

Pinel, J., Lovejoy, S., Schertzer, D., Tuck, A.F., 2012. Joint horizontal–vertical anisotropic scaling, isobaric and isoheight wind statistics from aircraft data. Geophys. Res. Lett. 39, L11803. http://dx.doi.org/10.1029/2012GL051689.

Puschell, J.J., Lowe, H.A., Jeter, J., Kus, S., Hurt, W.T., Gilman, D., Rogers, D., Hoelter, R., Ravella, R., 2002. Japanese Advanced Meteorological Imager: a next generation GEO imager for MTSAT-1R. SPIE Proc. 4814, 152–161.

Puschell, J.J., Lowe, H.A., Jeter, J., Kus, S., Osgood, R., Hurt, W.T., Gilman, D., Rogers, D., Hoelter, R., Kamel, A., 2003. Japanese Advanced Meteorological Imager (JAMI): design, characterization and expected on-orbit performance. Proceedings of International TOVS Study Conference, Sainte Adele, Canada.

Radkevich, A., Lovejoy, S., Strawbridge, K., Schertzer, D., 2007. The elliptical dimension of space–time atmospheric stratification of passive admixtures using lidar data. Physica A 382, 597–615. http://dx.doi.org/10.1016/j.physa.2007.03.046.

Radkevich, A., Lovejoy, S., Strawbridge, K., Schertzer, D., Lilley, M., 2008. Scaling turbulent atmospheric stratification, Part III: space–time stratification of passive scalars from lidar data. Q. J. R. Meteorol. Soc. 134, 316–335.

Sarachik, E.S., Cane, M.A., 2010. The El Niño-Southern Oscillation Phenomenon. Press (384 pp.).

Schertzer, D., Lovejoy, S., 1985a. Generalised scale invariance in turbulent phenomena. Phys. -Chim. Hydrodyn. J. 6, 623–635.

Schertzer, D., Lovejoy, S., 1985b. The dimension and intermittency of atmospheric dynamics. In: Launder, B. (Ed.), Turbulent Shear Flow 4. Springer-Verlag, Berlin, pp. 7–33.

Schertzer, D., Lovejoy, S., 1987. Physical modeling and analysis of rain and clouds by anisotropic scaling multiplicative processes. J. Geophys. Res. 92, 9692–9714.

Schertzer, D., Lovejoy, S., 1997. Universal multifractals do exist!: Comments on "A statistical analysis of mesoscale rainfall as a random cascade". J. Appl. Meteorol. 36, 1296–1303.

Schertzer, D., Lovejoy, S., Schmitt, F., 1995. Structures in turbulence and multifractal universality. In: Meneguzzi, M., Pouquet, A., Sulem, P.L. (Eds.), Small-scale structures in three-dimensional hydro and Magnetohydrodynamic turbulence. Lecture Notes in Physics, vol. 462. Springer-Verlag, Berlin, pp. 137–144.

Schertzer, D., Lovejoy, S., 2011. Multifractals, generalized scale invariance and complexity in geophysics. International Journal of Bifurcation and Chaos 21 (12), 3417–3456.

Schertzer, D., Tchigirinskaya, I., Lovejoy, S., Tuck, A., 2011. Quasi-geostrophic turbulence and generalized scale invariance, a theoretical reply. Atmos. Chem. Phys. Discuss. 11, 3301–3320 (201111/10).

Schertzer, D., Tchigirinskaya, I., Lovejoy, S., Tuck, A., 2012. Quasi-geostrophic turbulence and generalized scale invariance, a theoretical reply. Atmos. Chem. Phys. 12 (327–336), 2012. http://dx.doi.org/10.5194/acp-12-327-2012.

Stolle, J., Lovejoy, S., Schertzer, D., 2010. The stochastic cascade structure of deterministic numerical models of the atmosphere. Nonlinear Process. Geophys. 16, 607–621.

Stolle, J., Lovejoy, S., Schertzer, D., 2012. The temporal cascade structure and space–time relations for reanalyses and global circulation models. Q. J. R. Meteorol. Soc. 138, 1895–1913. http://dx.doi.org/10.1002/qj.1916.

Szantai, A., Seze, G., 2008. Improved extraction of low-level atmospheric motion vectors over west-Africa from MSG images. 9th International Winds Workshop, 14–18 April 2008, Annapolis, MD, USA, pp. 1–8.

Takeuchi, W., Nemoto, T., Kaneko, T., Yasuoka, Y., 2010. Development of MTSAT data processing, distribution and visualization system on WWW. Asian J. Geoinf. 10 (3), 29–33.

Taylor, G.I., 1938. The spectrum of turbulence. Proc. R. Soc. Lond. A 164 (919), 476–490. http://dx.doi.org/10.1098/rspa.1938.0032.

Tennekes, H., 1975. Eulcrian and Lagrangian time microscales in isotropic turbulence. J. Fluid Mech. 67, 561–567.

Walker, G.T., Bliss, E.W., 1930. World weather IV. Mem. R. Meteorolog. Soc. 3 (24), 81–95.

Walker, G.T., Bliss, E.W., 1932. World weather V. Mem. R. Meteorolog. Soc. 4 (36), 53–84.

Walker, G.T., Bliss, E.W., 1937. World weather VI. Mem. R. Meteorolog. Soc. 4 (39), 119–139.

Wheeler, M., Kiladis, G.N., 1999. Convectively coupled equatorial waves: analysis of clouds and temperature in the wavenumber–frequency domain. J. Atmos. Sci. 56, 374–399.

Yano, J., 2009. Comment on "Reinterpreting aircraft measurments in anisotropic scaling turbulence" by Lovejoy et al 2009. Atmos. Chem. Phys. Discuss. 9, S162–S166.

Please cite this article as: Pinel, J., et al., The horizontal space–time scaling and cascade structure of the atmosphere and satellite radiances, Atmos. Res. (2014), http://dx.doi.org/10.1016/j.atmosres.2013.11.022